Spatial slip rate distribution along the SE Xianshuihe fault, eastern Tibet, and earthquake hazard assessment

Mingkun Bai[1], Marie-Luce Chevalier[1], Philippe Hervé Leloup[2], Haibing Li[1], Jiawei Pan[3], Anne Replumaz[4], Shiguang Wang[5], kaiyu li[1], Qiong Wu[1], fucai liu[1], and Jinjiang Zhang[6]

[1]Institute of Geology, Chinese Academy of Geological Sciences
[2]Laboratoire de géologie de Lyon, Université de Lyon 1
[3]Institute of Geology
[4]ISTerre, Université Grenoble Alpes
[5]National Institute of Natural Hazards, Ministry of Emergency Management of China
[6]Peking University

November 26, 2022

Abstract

The Xianshuihe (XSH) fault in eastern Tibet is one of the most active faults in China, with the next large earthquake most likely to occur along its SE part, where the fault splits into three parallel branches: Yalahe, Selaha and Zheduotang. Precisely quantifying their slip rates at various timescales is essential to evaluate regional earthquake hazard. Here, we expand our previous work on the Selaha fault, to the nearby Zheduotang and Moxi faults, and add observations on the Yalahe fault and on the newly discovered Mugecuo South fault zone. Using tectonic-geomorphology approaches with 10Be dating, we had determined average late Quaternary slip rates of 9.75±0.15 and 4.4±0.5 mm/yr along the NW and SE Selaha fault, respectively. Using the same methods here, we determine a slip rate of 3.7-5.4 mm/yr on the Zheduotang fault and of 10.4-14.8 mm/yr on the Moxi fault. This is consistent with the southeastward slip rate increase we had proposed along the XSH fault system from 6-8 mm/yr (Ganzi fault) to ~10 mm/yr (Selaha fault), and >10.4 mm/yr (Moxi fault). We eventually propose a new model for the SE Xianshuihe fault, where the large-scale Mugecuo pull-apart basin lies within an even larger scale compressive uplift zone in the XSH fault's restraining bend, where the highest peak in eastern Tibet is located (Gongga Shan, 7556 m). Our slip rates determination allows to estimate a relatively high regional earthquake hazard of Mw~7 at present in the SE Xianshuihe fault.

Hosted file

`bai-si.docx` available at https://authorea.com/users/545450/articles/606418-spatial-slip-rate-distribution-along-the-se-xianshuihe-fault-eastern-tibet-and-earthquake-hazard-assessment

Hosted file

`bai-tectonics-r1.docx` available at https://authorea.com/users/545450/articles/606418-spatial-slip-rate-distribution-along-the-se-xianshuihe-fault-eastern-tibet-and-earthquake-hazard-assessment

1

1 **Spatial slip rate distribution along the SE Xianshuihe fault, eastern Tibet, and**

2 **earthquake hazard assessment**

3

4 Mingkun Bai[1,2], Marie-Luce Chevalier[1,3*], Philippe Hervé Leloup[4], Haibing Li[1,3], Jiawei Pan[1,3],

5 Anne Replumaz[5], Shiguang Wang[6,1], Kaiyu Li[1], Qiong Wu[1], Fucai Liu[1], Jinjiang Zhang[2]

6

7 [1] Key Laboratory of Deep-Earth Dynamics of Ministry of Natural Resources, Institute of Geology,

8 Chinese Academy of Geological Sciences, 26 Baiwanzhuang Rd, Beijing 100037, People's

9 Republic of China

10 [2] Ministry of Education Key Laboratory of Orogenic Belts and Crustal Evolution, School of Earth

11 and Space Sciences, Peking University, Beijing 100871, People's Republic of China

12 [3] Southern Marine Science and Engineering Guangdong Laboratory (Guangzhou), Guangzhou

13 511458, People's Republic of China

14 [4] Laboratoire de géologie de Lyon, CNRS UMR 5570, Université de Lyon, Villeurbanne, France

15 [5] ISTerre, Université Grenoble Alpes, CNRS, Grenoble, France

16 [6] National Institute of Natural Hazards, Ministry of Emergency Management of China, Beijing,

17 China

18

19 **Highlights**

*Corresponding author : Marie-Luce Chevalier (mlchevalier@hotmail.com), Tel: +86 13466654223

20 -We determined late Quaternary slip rates of 3.7-5.4 and 10.4-14.8 mm/yr along the Zheduotang

21 and Moxi segments, respectively

22 -We suggest a SE rate increase along the Xianshuihe fault system from Ganzi to Moxi

23 -We discovered a new active fault (Mugecuo South) between Selaha and Zheduotang segments, a

24 large-scale pull-apart within an uplift zone

25

26 **Abstract**

27   The Xianshuihe (XSH) fault in eastern Tibet is one of the most active faults in China, with

28 the next large earthquake most likely to occur along its SE part, where the fault splits into three

29 parallel branches: Yalahe, Selaha and Zheduotang. Precisely quantifying their slip rates at various

30 timescales is essential to evaluate regional earthquake hazard. Here, we expand our previous work

31 on the Selaha fault, to the nearby Zheduotang and Moxi faults, and add observations on the Yalahe

32 fault and on the newly discovered Mugecuo South fault zone. Using tectonic-geomorphology

33 approaches with ^{10}Be dating, we had determined average late Quaternary slip rates of 9.75±0.15 and

34 4.4±0.5 mm/yr along the NW and SE Selaha fault, respectively. Using the same methods here, we

35 determine a slip rate of 3.7-5.4 mm/yr on the Zheduotang fault and of 10.4-14.8 mm/yr on the Moxi

36 fault. This is consistent with the southeastward slip rate increase we had proposed along the XSH

37 fault system from 6-8 mm/yr (Ganzi fault) to ~10 mm/yr (Selaha fault), and >10.4 mm/yr (Moxi

38 fault). We eventually propose a new model for the SE Xianshuihe fault, where the large-scale

39 Mugecuo pull-apart basin lies within an even larger scale compressive uplift zone in the XSH

40 fault's restraining bend, where the highest peak in eastern Tibet is located (Gongga Shan, 7556 m).

41 Our slip rates determination allows to estimate a relatively high regional earthquake hazard of

42 Mw~7 at present in the SE Xianshuihe fault.

43

Plain Language Summary

The Xianshuihe fault in eastern Tibet is one of the most active faults in China, with the next large earthquake most likely to occur along its southeastern part, where the fault zone consists of four parallel branches with complicated geometries. Studying the activity and slip rate of each branch is essential to evaluate regional earthquake hazard, especially because they cross a major city (Kangding), and because of the imminent construction of the Chengdu-Lhasa railroad. Here, we expand our previous slip rate study on one fault branch (Selaha) to two additional ones (Zheduotang and Moxi), together with key observations on the newly discovered 'Mugecuo South fault zone'. We find that the rate over the last ~100,000 years may increase southeastwards along the Xianshuihe fault system, as previously suggested. The fast slip rates and their complex spatial distribution in the Kangding region reveal a high earthquake hazard (Mw~7) at present.

1. Introduction

The eastern margin of the Tibetan Plateau is an important, active tectonic boundary with numerous active faults which accommodate slip due to the eastward motion of the plateau (e.g., Tapponnier and Molnar, 1977; Wang et al., 1998; Wang and Burchfiel, 2000; Han et al., 2019) (Fig. 1). This region belongs to the "eastern Tibet seismic belt" or "N-S tectonic zone" (Deng et al., 2003; Zhang, 2013) along which an extremely large number of M>7 earthquakes occurred. In particular, along the NW-striking, ~1400 km-long, left-lateral Xianshuihe (hereafter XSH) fault system, as many as 17 M>7 and 29 M>6.5 earthquakes have ruptured almost its entire length since 1700, with three M>7.3 earthquakes along just the XSH segment since 1923 (Allen et al., 1991; Wen, 2000) (Fig. 2A). Following two large earthquakes nearby (2008 Mw7.9 Wenchuan and 2013 Ms7 Lushan, Fig. 1), the seismic risk near Kangding city is believed to have increased by a factor of two, attested by Coulomb stress increase (e.g., Parsons et al., 2008; Toda et al., 2008; Shan et al., 2009, 2013; Nalbant and McCloskey, 2011; Yang et al., 2015; Guo et al., 2018; Xu et al., 2019), which was only

69   partly reduced after the 2014 Kangding earthquake sequence (Mw5.9 and 5.6) (Jiang et al 2015a;

70   Bai et al., 2018) (Fig. 2A). This region is now widely accepted as a seismic gap (e.g., Allen et al.,

71   1991; Wen, 2000; Wen et al., 2008; Jiang et al., 2015a; Shao et al., 2016; Wang and Shen, 2020; Li

72   and Bürgmann, 2021), where a large earthquake would be tragic because of casualties (Kangding

73   city has a population of ~150,000) and infrastructure damages not only due to ground shaking but

74   also because of landslides and mud flows on the very steep surrounding slopes.
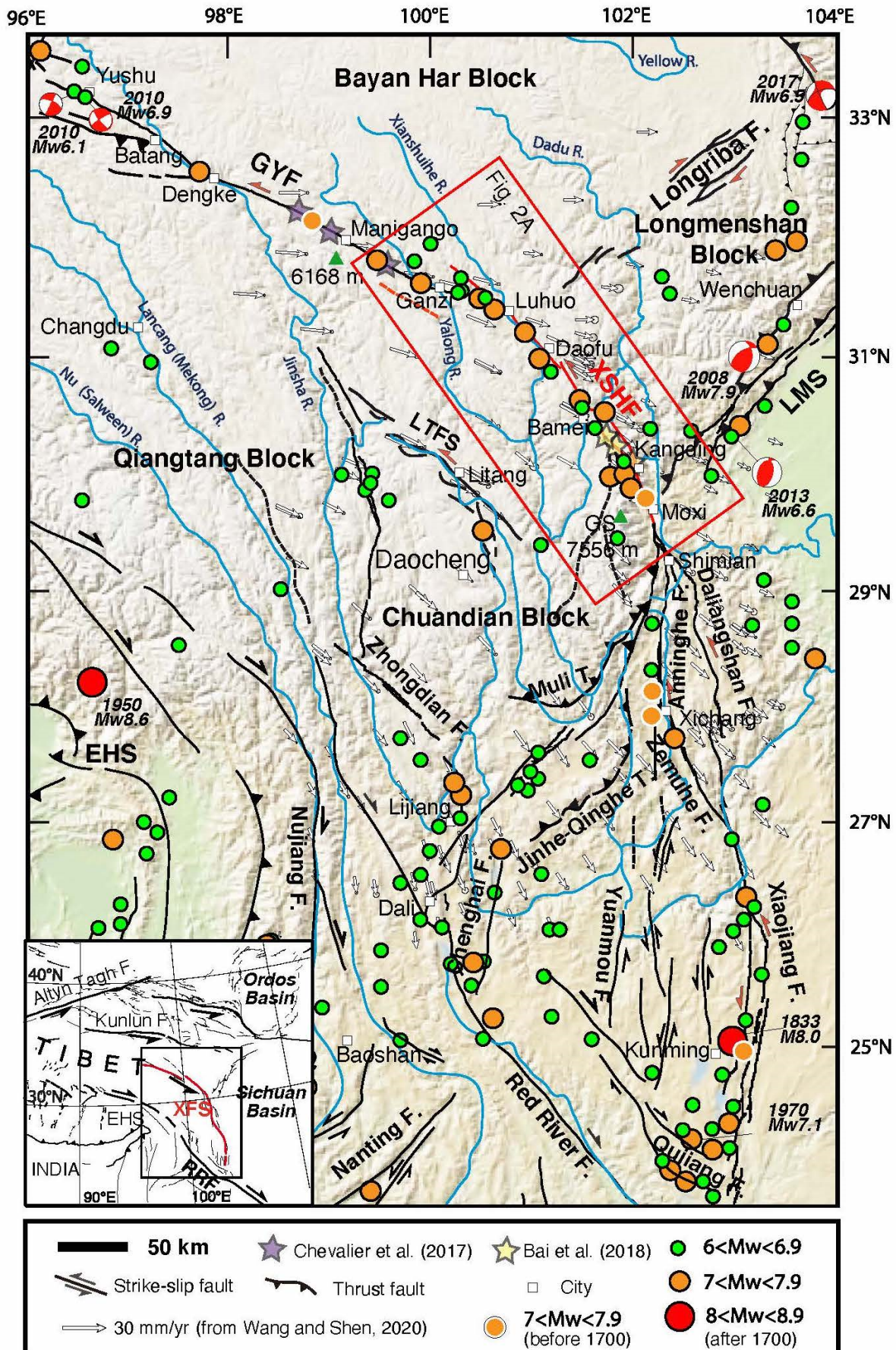
96°E · 98°E · 100°E · 102°E · 104°E

Bayan Har Block

Yellow R.
Yushu · 2010 · Mw6.9
2010 · Mw6.1
Batang
Dengke
GYF
Manigango
6168 m
Changdu
Lancang (Mekong) R.
Nu (Salween) R.
Jinsha R.
Yalong R.
Xianshuihe R.
Dadu R.
Fig. 2A
Ganzi · Luhuo
Daofu
XSHF
Bamei · Kangding
Longriba F.
2017 · Mw6.5
Longmenshan Block
Wenchuan
2008 · Mw7.9
LMS
2013 · Mw6.6

Qiangtang Block

LTFS
Litang
Daocheng
Chuandian Block
GS · 7556 m
Moxi
Shimian
Daliangshan F.

1950 · Mw8.6
EHS
Zhongdian F.
Muli T.
Anninghe F.
Xichang
Nujiang F.
Lijiang
Jinhe-Qinghe T.
Yuanmou F.
Zemuhe F.
Xiaojiang F.
Dali
Chenghai F.
Baoshan
Red River F.
Kunming
1833 · M8.0
Nanting F.
Qujiang
1970 · Mw7.1

33°N
31°N
29°N
27°N
25°N

[Inset map:]
40°N
Altyn Tagh F.
Kunlun F.
Ordos Basin
TIBET
30°N
EHS
XFS
Sichuan Basin
INDIA
RRF
90°E · 100°E

50 km
Strike-slip fault
30 mm/yr (from Wang and Shen, 2020)
Chevalier et al. (2017)
Thrust fault
Bai et al. (2018)
City
6<Mw<6.9
7<Mw<7.9
7<Mw<7.9 (before 1700)
8<Mw<8.9 (after 1700)

75

76 ***Figure 1:*** *Xianshuihe fault system (XFS) within India–Asia collision zone. Tectonic map of SE Tibet*

77 *with digital elevation model (DEM) in background. Horizontal GPS velocity field with respect to*

78 *stable Eurasian plate (Wang and Shen, 2020), focal mechanisms of instrumental, Mw>6*

79 *earthquakes (Global Harvard CMT catalog 1976–2020) (2008 Wenchuan, 2010 Yushu, 2013*

80 *Lushan and 2017 Jiuzhaigou), as well as earthquakes from USGS and CEA (1995), main peaks,*

81 *cities, active faults (those of Xianshuihe fault in red), tectonic blocks and rivers.*

82 *LMS=Longmenshan, GYF=Ganzi-Yushu fault, XSHF=Xianshuihe fault, LTFS=Litang fault system,*

83 *GS=Gongga Shan. Inset shows the XFS within Asia, EHS=Eastern Himalayan Syntaxis, RRF=Red*

84 *River fault.*

85

86
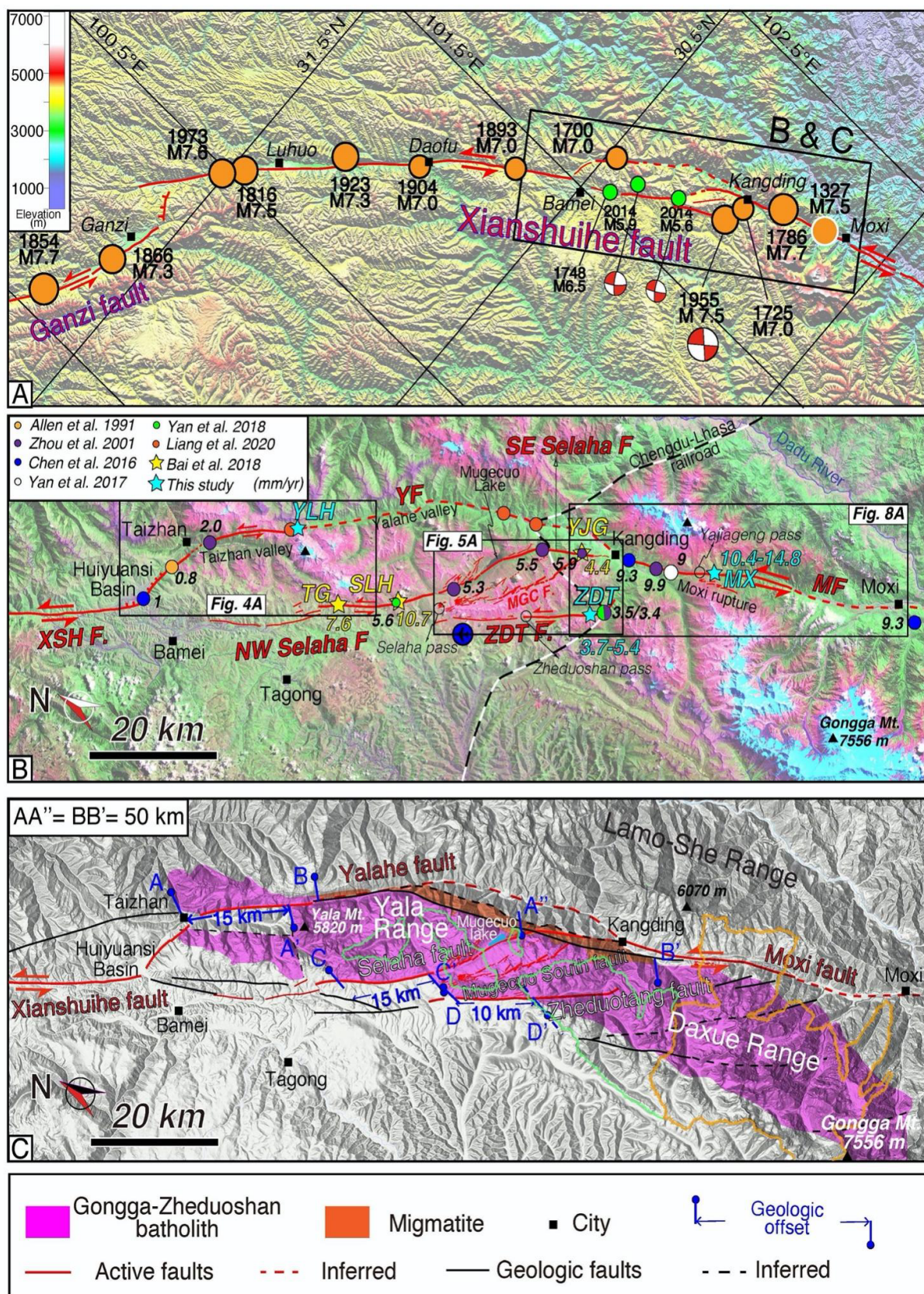
Figure 2: Xianshuihe (XSH) fault. (A) Post 1700 A.D. M>7 earthquakes distribution (+ that of

1327 near Moxi) (e.g., USGS, Wen et al., 2008; Cheng et al., 2011) along XSH and SE Ganzi faults.

98

99   Near Kangding city, the linear XSH fault splits into three right-stepping, en-echelon segments:

100   Yalahe, Selaha and Zheduotang, before reconnecting as the Moxi segment (Fig. 2B). In order to

101   better understand the complicated tectonics of this particularly active region of eastern Tibet, and

102   assess its seismic hazard, precisely constraining the slip-rates of the several regional active fault

103   branches is essential. While Bai et al. (2018) determined the Selaha fault's late Quaternary

104   horizontal slip-rate at three locations, in this paper, we constrain that of two other regional fault

105   segments (Zheduotang and Moxi) using similar approaches (see method section). We also present

106   preliminary observations on the activity of the central Yalahe segment, as well as of that of the

107   newly discovered 'Mugecuo South' fault zone located between the Selaha and Zheduotang

108   segments, which documents significant extension. Finally, we discuss the rates distribution in the

109   Kangding region of the SE XSH fault in the framework of eastern Tibet and compare them with

110   those from other regional studies at all timescales. We eventually propose a model for the SE XSH

111   fault where a large-scale pull-apart basin (Mugecuo) lies within an even larger scale restraining

112   bend where the highest peak in eastern Tibet is located (Gongga Shan, 7556 m), and assess regional

113   seismic hazard using the slip rates we determined. Our work also provides valuable data to the

114   highly challenging Chengdu-Lhasa railroad construction, which will cross all fault segments

115   discussed here (Fig. 2B).

116

2. Geological setting

117

118   The XSH fault system consists of four main left-lateral strike-slip fault segments which

119   separate the Bayan Har and Qiangtang/Chuandian blocks to the NE and SW, respectively:

120   Yushu/Batang at the NW end (where the 2010 Mw6.9 Yushu earthquake occurred), Ganzi in the

121   NW, XSH and Moxi in the center, and Anninghe-Zemuhe-Xiaojiang in the SE (Fig. 1). In the

122   Kangding region, the Yalahe, Selaha and Zheduotang segments follow geological faults that left-

123   laterally offset the Gongga-Zheduoshan granite batholith (Chen et al., 1985) (Fig. 2C) and may be

124   connected at depth (e.g., Allen et al., 1991; Jiang et al., 2015a; Li et al., 2020). While the Selaha and

125   Zheduotang faults show evidence of recent activity along most of their traces, with numerous

126   scarps, sag ponds, and left-lateral (with minor vertical) offsets of mostly moraines and gullies, such

127   clear evidence seemed to be lacking along the Yalahe fault where it is parallel to the Selaha fault

128   (Allen et al., 1991; Bai et al., 2018).

129

2.1. Slip rates review

130

131   As slip-rates may vary temporally and/or spatially along a particular fault (e.g., Friedrich et

132   al., 2003; Chevalier et al., 2005), it is important to estimate them at various timescales as

133   summarized below as well as in Figure 3 and Table 1, from a few tens of years (using geodetic

134   techniques such as GPS/GNSS [Global Satellite Navigation System] or InSAR [Interferometric

135   Synthetic Aperture Radar]), to a few tens of ka (using tectonic-geomorphology approaches), to a

136   few Ma (using geologic tools).

2.1.1. Geologic timescale

138   Geologic rate estimates along the XSH fault vary between ~3.5 and 30 mm/yr, depending on

139   whether the ~60 km geologic offset of several markers (Jinsha and Xianshui Rivers, Proterozoic and

140   Permo-Triassic basement rocks, main Cenozoic thrusts) (e.g., Wang et al., 1998; Wang and

141   Burchfiel, 2000; Yan and Lin, 2015) is matched with initiation ages that vary from 2 to 19 Ma (e.g.,

142   Roger et al., 1995; Wang et al., 1998; Wang et al., 2012; Zhang, 2013; Yan and Lin, 2015; Zhang et

143   al., 2017).

144

146   ***Figure 3:*** *Summary of left-lateral slip rates along Xianshuihe and Moxi faults versus time (A) and*

147 *location along strike (B). See Table 1 for references to numbers. Colors represent rates along*

148 *different segments. Plain symbols represent our rates (this study as well as that of Bai et al., 2018).*

149 *(B) Grey shaded areas represent the best constrained late Quaternary rates for each main section of*

150 *the XSH fault: Ganzi, NW XSH, SE XSH, and Moxi faults (see discussion section). (C) Fault trace,*

151 *main cities and location of our study sites (blue stars: this study; yellow stars: Bai et al., 2018),*

152 *with best constrained late Quaternary slip rates in red (that of Ganzi from Chevalier et al., 2017).*

153

154 ***Table 1:*** *Slip rate summary along Xianshuihe fault*

Segment	Slip-rate (mm/yr)	Reference	Method	Ref. in Fig. 3
XSH fault	*9 - 12*	Wang et al. (2009)	InSAR near Luhuo	1
	12.2 - 13	W. Wang et al. (2017)	GPS - block model	2
	10 - 11	Shen et al. (2005)	GPS - rigid blocks	3
	12.7 - 15.9	Y. Wang et al. (2017)	GPS - block model	4
	8 - 10.2	Zheng et al. (2017)	GPS - profiles	5
	9 - 12	Ji et al. (2020)	InSAR - interseismic deformation	6
	10 - 15	Zhang et al. (2019)	InSAR - dislocation model	7a
	8.1-11.1	Qiao and Zhou (2021)	InSAR	7b
	7.67 - 9.13	Li et al. (2019)	Gravity + GPS (Luohuo-Qianning)	8a
	3.4 - 5.6	Li et al. (2020)	GPS + earthquake relocation (Daofu-Qianning)	9a
	14.4	Gan et al. (2007)	GPS - dislocation	10a
	13.6-15.4	Wang et al. (2020)	GPS - elastic block model	10b
	7 - 10.3	Jiang et al. (2015b)	3D visco-elastic model with InSAR and GPS data	11a
	10 - 20	Allen et al. (1991)	inferred ages	12a
	8 - 11	Zhang (2013)	reinterpretation of Chen et al. (2008), using upper terrace age	13a
	8.4	Liang et al. (2020)	14C - Paleoearthquake 3 ka (Luhuo)	14
	7.5 - 11.1	Zhang (2013)	90 - 100 km in 10 Ma	13b
	15 - 30	Wang et al. (1998)	60 km in 2-4 Ma	15
	~4.5	Roger et al. (1995)	62 km in 13 Ma (Bai et al., 2018)	16
	4.6 - 12	Yan and Lin (2015)	62 km in 5-13 Ma	17
	~3.5	Wang et al. (2012)	62 km in 17±2 Ma (Bai et al., 2018)	18
	6.8 - 7.6	Zhang et al. (2017)	62 km since 8.6±0.5 Ma	19a
Yalahe fault	*0.8 - 3.8*	Li et al. (2020)	GPS + earthquake relocation	9b

	0.8	Allen et al. (1991)	inferred ages	12b
	1.8 - 2.2	Zhou et al. (2001)	one TL age - paleoseimology	20a
	0.6 - 1.5	Chen et al. (2016)	TL ages - tectonic geomorphology	21a
Selaha fault	*6.14*	Li et al. (2019)	Gravity + GPS data	8b
	5.9 - 9.1	Li et al. (2020)	GPS + earthquake relocation	9c
	4.9 - 6.1	Zhou et al. (2001)	TL and 14C ages - paleoseimology	20b
	9.6 - 9.9	**Bai et al. (2018)**	**10Be (TG and SLH sites, NW Selaha fault)**	**22a**
	3.9 - 4.9	**Bai et al. (2018)**	**10Be (YJG site, SE Selaha fault)**	**22b**
	4.8 - 6.4	Yan et al. (2018)	14C - tectonic geomorphology	23a
	5.7 - 6.9	Zhang et al. (2017)	25 km since 4±0.4 Ma (Bai et al., 2018)	19b
Zheduotang fault	*0.4 - 3.4*	Li et al. (2020)	GPS + earthquake relocation	9d
	3.2 - 3.8	Zhou et al. (2001)	14C - paleoseimology	20c
	3 - 3.8	Yan et al. (2018)	14C - tectonic geomorphology	23b
	3.7 - 5.4	**This study**	**10Be (ZDT site)**	**ZDT**
Yalahe/Selaha/Zheduotang	*~11*	Wang and Shen (2020)	GPS - profiles	24a
	8.8-16	Qiao and Zhou (2021)	InSAR	7c
Moxi fault	*7 - 12.7*	Jiang et al. (2015b)	3D visco-elastic model with InSAR and GPS data	11b
	4.41	Li et al. (2019)	Gravity and GPS data	8c
	~13	Wang and Shen (2020)	GPS - profiles	24b
	16.5-19.3	Qiao and Zhou (2021)	InSAR	7d
	9.3 - 10.5	Zhou et al. (2001)	14C - paleoseimology	20d
	8.3 - 10.3	Chen et al. (2016)	14C - tectonic geomorphology	21b
	~9	Yan et al. (2017)	14C - paleoseimology	25
	10.4 - 14.8	**This study**	**10Be (MX site)**	**MX**

155

2.1.2. Late Quaternary timescale

A growing body of evidence now suggests a slip rate of ~10 mm/yr for the XSH fault (e.g.,
Zhang, 2013; Bai et al., 2018). Bai et al. (2018) suggested that the southeastward rate increase
between the Ganzi fault (~6-8 mm/yr, Chevalier et al., 2017) and the XSH fault may be linked to
the interaction with the nearby NE-striking, reverse/dextral Longriba fault system to the north, as
recently endorsed by a recent GPS study (Wang et al., 2020). This fault indeed marks the limit
between the fast-moving Bayan Har block to the NW and the slow-moving Longmenshan block to

163   the SE, as observed in GPS data when considered relative to stable Eurasia (e.g., W. Wang et al.

164   2017, 2020; Y. Wang et al., 2017; Wang and Shen, 2020) (Fig. 1).

165   What occurs in the Kangding region however, where the fault splits into three segments, is

166   more complex. While the NW Yalahe fault, with a normal/left-lateral sense consistent with its

167   oblique direction compared to the general trend of the geologic fault, may slip at ~0.6 to 2.2 mm/yr

168   (Allen et al., 1991; Zhou et al., 2001; Chen et al., 2016, Figs. 2B, 3, and Table 1), no rates have yet

169   been determined farther to the SE. Along the NW Selaha fault (west of the Selaha pass, Fig. 2B),

170   slip rates had been inferred to range between 3.7 and 9.7 mm/yr (Allen et al., 1991; Chen et al.,

171   2016) and were estimated (using ^{14}C dating) as ranging from 4.8 to 6. 4 mm/yr (Zhou et al., 2001;

172   Yan et al., 2018). More recently, Bai et al. (2018) studied two sites along the NW Selaha fault (TG

173   and SLH) and one site along its SE part (YJG) (yellow stars in Fig. 2B). Using ^{10}Be dating and

174   offset-age reconstructions, they determined slip-rates of 7.6(+2.3/−1.9) mm/yr at TG and

175   10.7(+1.3/−1.1) mm/yr at SLH, hence 9.6 - 9.9 mm/yr assuming that the rate should be similar at

176   these two sites located only 9 km apart. At YJG, located along the SE Selaha fault, Bai et al. (2018)

177   determined a much lower rate of 3.9 - 4.9 mm/yr. This led them to infer a rate of ~5 mm/yr on the

178   parallel Zheduotang fault, corresponding to the difference between rates along the NW and SE

179   Selaha fault. Other studies on the Zheduotang fault suggested slip-rates of 3 to 3.8 mm/yr (Zhou et

180   al., 2001; Yan et al., 2018) (Figs. 2B, 3, and Table 1).

181   The linear and continuous, ~50 km-long, Moxi fault located SE of Kangding, merges with the

182   Selaha fault (Allen et al., 1991; Jiang et al., 2015a; Bai et al., 2018). Most studies used ^{14}C dating

183   from trenches located <9 km from Kangding, NW of the Yajiageng (or Xuemenkan) pass (Fig. 2B),

184   to determine late Quaternary slip-rates along the Moxi fault of ~8.3-10.5 mm/yr (e.g., Zhou et al.,

185   2001; Chen et al., 2016; Yan et al., 2017).

186   **2.1.3. Geodetic timescale**

187   At the geodetic timescale, InSAR (7-15 mm/yr, e.g., Wang et al., 2009; Jiang et al., 2015b;

188   Zhang et al., 2019; Ji et al., 2020; Qiao and Zhou, 2021) and GPS (8-15.9 mm/yr, e.g., Shen et al.

189   2005; Gan et al., 2007; W. Wang et al., 2017, 2020; Y. Wang et al., 2017; Zheng et al., 2017; Li et

190   al., 2019) rates along the XSH fault (Fig. 3 and Table 1) are widespread but encompass the late

191   Quaternary rates. Note however that estimates based on the longest GPS record (Zheng et al., 2017)

192   suggest a rate of ~8 to 10.2 mm/yr. At a more detailed level, GPS rates vary between 0.8 and 3.8

193   mm/yr along the Yalahe fault (Li et al., 2020), 5.9-9.1 mm/yr along the Selaha fault (Li et al., 2019;

194   Li et al., 2020), 0.4-3.4 mm/yr along the Zheduotang fault (Li et al., 2020) and 4.41-19.3 mm/yr

195   along the Moxi fault (Jiang et al., 2015b; Li et al., 2019; Wang and Shen, 2020; Qiao and Zhou,

196   2021). Two recent studies recently suggested rates of ~11 mm/yr (Wang and Shen, 2020) and 8.8-16

197   mm/yr (Qiao and Zhou, 2021) across the three branches (Yalahe/Selaha/Zheduotang) of the SE

198   XSH fault (Fig. 3 and Table 1).

199

200   **2.2. Past earthquakes in the Kangding region**

201   One M7.0 earthquake in 1700 has been reported along the Yalahe fault with ~41 km of surface

202   ruptures (Wen, 2000; Wen et al., 2008) (Fig. 2A). Two historical earthquakes, M7.0 in 1725 and

203   M6.5 in 1748, have both been inferred to have ~40 km of surface ruptures along the SE and NW

204   Selaha fault, respectively, the former being however poorly constrained (Wen, 2000; Wen et al.,

205   2008; Papadimitriou et al., 2004). The recent 2014 Mw5.9 and 5.6 Kangding earthquake sequence

206   also mostly shook the NW part of that fault (e.g., Jiang et al., 2015a). Along the Zheduotang fault,

207   the 1955 Mw7.5 Kangding earthquake produced 35 km of surface ruptures (Wen, 2000; Wen et al.,

208   2008; Zhou et al., 2001; Papadimitriou et al., 2004), although it has recently been re-evaluated by

209   Yan et al. (2019) as only Mw7.0 with 43 km of surface ruptures that extend farther SE towards

210   Moxi ('Moxi rupture' in Fig. 2B). Along the Moxi fault, two large M7.5 and M7.7 earthquakes

211   occurred in 1327 and 1786, respectively, the latter having produced 70-90 km of surface ruptures

212   and 2-5 m of co-seismic offsets (Zhou et al., 2001; Wen et al., 2008; Cheng et al., 2011). It also

213   yielded a landslide dam across the nearby Dadu River, whose rupture ten days later following a

214   strong aftershock, caused one of the most disastrous landslide dam failure in the world with

215   ~100,000 casualties (e.g., Dai et al., 2005).

216

217   **3. Methods**

218   We used field investigation, as well as Google Earth and Bing high-resolution satellite

219   imagery to map active fault strands and offset geomorphic features along the Zheduotang and Moxi

220   fault segments of the SE XSH fault near Kangding. We could then select the best sites with limited

221   signs of erosion and clear piercing points across the fault in order to precisely measure the

222   cumulative offsets. In this high elevation and high-relief region (with slopes up to 35° along the

223   Zheduotang fault and 15° along the Moxi fault at our study sites), moraines and gullies are the most

224   commonly observed offset markers, in addition to related sag ponds and fault scarps. Good sites are

225   scarce. We selected the best two sites along the fault segments to conduct our study: the Zheduotang

226   (ZDT) and Moxi (MX) moraines. That their crests are sub-rounded and oblique to the fault results

227   in larger offset uncertainties, that we precisely measure on high-resolution Digital Elevation Models

228   (DEM) obtained from Unmanned Aerial Vehicle (UAV aka drone, DJI Phantom 4 Pro) surveys at

229   both sites, and from additional surveys using a Riegel VZ1000 terrestrial LiDAR (Light Detection

230   and Ranging) (angular resolution of 0.02° for raw data, set to 0.5 m between two data points after

231   process) at the MX site. Offset values and their uncertainties were obtained by repeatedly realigning

232   the offset moraine crests to their best original fit on the DEM. Note that along a left-lateral fault,

233   offsets on the left bank best represent the total offset, as that on the right bank may suffer

234   continuous lateral erosion thus only yielding a minimum offset.

235   We therefore collected a total of 25 samples along the crests on the left bank: nine samples

236   from the lateral moraine crest at the ZDT site and 11 from that at the MX site. These samples were

237 collected from the top few centimeters of large, stable, well-embedded granite boulders (1-4 m in

238 diameter, Figs. S1-S2) using chisel and hammer. Collecting numerous (>6) samples on individual

239 moraine crests has long been our team's moto, which greatly increases the likelihood to date the

240 actual abandonment age of the moraine (Chevalier et al., 2011; Chevalier and Replumaz, 2019).

241 Because moraines can only become stable after the ice retreats, their ages represent abandonment

242 ages thus onset age of deglaciation.

243   We use cosmogenic ^{10}Be surface-exposure dating (e.g., Lal, 1991; Gosse and Phillips, 2001)

244 to constrain the moraine abandonment ages following mineral separation and quartz cleaning

245 procedure modified from Kohl and Nishiizumi (1992). ^{10}Be concentrations mostly come from

246 nuclide accumulation from exposure to cosmic rays at the site. Model ages were calculated using

247 CRONUS v3 (Balco et al., 2008) with the Lm (Lal [1991]/Stone [2000], time-dependent) and LSDn

248 (Lifton et al., 2014, time-dependent) production rate models (Table 2) and we refer to the Lm ages

249 in the text. We then combine the moraines abandonment age with their offsets to reconstruct the

250 space-time evolution of the Zheduotang and Moxi faults and determine their late Quaternary

251 average slip-rates. We report the latter as median rates (with uncertainties at the 68.27% confidence

252 interval about the median) obtained using the Gaussian uncertainty model of Zechar and Frankel

253 (2009).

254   Ideally, one wants to sample boulders that have been exposed on moraine crests since

255 deglaciation, with no rolling, shielding or surface erosion since deposition (which would tend to

256 skew the ages toward values younger than the actual age), and no exposure prior to deposition

257 (which would tend to skew ages toward older values). These old ages however, are thought to be

258 occasional (e.g., Hallet and Pukonen, 1994; Putkonen and Swanson, 2003; Heyman et al., 2011),

259 especially since rocks have been pulled off from the glacial valley by the glacier, crushed, and

260 eroded before resting on a moraine's crest. Such outliers may be singled out and discarded using

261 statistical tests such as Chauvenet (Bevington and Robinson, 2002) or Peirce criteria. Four (three

262 young and one old) outliers were found on MX main crest and two old ones on ZDT crest. After

263 rejecting them, and following Heyman (2014), we assign a class (A for well-, B for moderately- and

264 C for poorly- clustered ages) to each moraine, using reduced Chi-square analyses (also see

265 Chevalier and Replumaz, 2019). While the average age is taken to represent the most likely

266 abandonment age of Class A moraines, the oldest age is instead taken for Classes B and C moraines

267 (Heyman, 2014) because even though moraines are relatively stable landforms over the long term,

268 crests are slowly adjusting following their abandonment, with boulders being gradually exhumed to

269 the surface (hence their younger ages), thus representing multiple stages of exhumation as the

270 surface lowers due to erosion of the matrix (e.g., Chevalier and Replumaz, 2019). Therefore, and

271 because we assume zero erosion and did not correct for potential snow and vegetation cover, the

272 apparent ages we calculate are minimum ages. Eventually, we assign a Marine oxygen Isotope

273 Stage (MIS) (e.g., Lisiecki and Raymo, 2005) to each moraine which indicates the climatic period

274 during which the moraine was abandoned.

275

276 **4. Sites description and results**

277 We describe the faults and study sites from NW to SE along the SE XSH fault (Fig. 2B).

278 First, we introduce our preliminary results attesting to the central Yalahe fault activity, just north of

279 Yala Mountain (Fig. 4), then describe the newly discovered 'Mugecuo South' fault zone (Fig. 5)

280 located on the NE flank of the Zheduoshan Range between the Selaha and Zheduotang faults. We

281 then present the two study sites, ZDT moraine along the Zheduotang fault (Figs. 6, 7) and MX

282 moraine along the Moxi fault (Figs. 7, 8).

283

284 **4.1. Yalahe fault**

285 The Yalahe fault constitutes the NE branch of the right-stepping, en-echelon faults of the

active SE XSH fault (Fig. 2B). It runs from the eastern Huiyuansi basin where it strikes N108°E,

cuts across the slopes of Taizhan valley and merges with the N141°E-striking Yalahe geologic fault

along the northern side of Yala Mountain (peak at 5820 m), where it more or less follows the Yalahe

valley for ~18 km until it reaches Kangding city (Fig. 2B,C). The Yalahe geologic fault extends

~130 km NW of Taizhan before merging with the XSH fault. Near Taizhan, the granitoids are

affected by a ~1.3 km-wide zone of ductile and brittle deformation linked to the left-lateral Yalahe

fault (Chen et al., 1985). The northern boundary of the Gongga-Zheduoshan batholith shows an

apparent minimum offset of 15 km (AA' in Fig. 2C), but the offset of the southern boundary may be

as large as 50 km (Bai et al., 2018) (AA'' and BB' in Fig. 2C).

The active NW part of the Yalahe fault bounds the SE Huiyuansi basin, which was created

thanks to the significant oblique (left-lateral/normal) component of motion along that segment, in

agreement with its oblique strike direction compared to that of the main XSH fault (e.g., Allen et al.

1991) (Fig. 2B). Aerial photograph analyses (Allen et al., 1991) and field investigation (Liang et al.,

2020) show that the central part of the fault between ~Taizhan and Yala Mountain has a clear trace

suggesting that it is also active. The fault can be followed for ~7 km on satellite images, and during

our own field investigation, we found a ~1 m-high fault scarp along ~2.4 km of the fault (Fig. 4),

i.e., a total of at least ~10 km, as recently reported by Liang et al. (2020), who also found several

co-seismic (2.5-3.5 m) as well as one cumulative (~15 m) horizontal offsets along that central

section. Just SE of Yala Mountain however, in the large U-shaped Yalahe valley (Fig. 4B), the fault

trace cannot easily be followed on satellite images, either because this section may be inactive at

present with activity having been transferred to the Selaha fault (e.g., Zhang et al., 2017; Bai et al.,

2018), or because of the dense vegetation making remote sensing analyses difficult. Extra field

work is clearly necessary to constrain the behavior of the Yalahe fault along its SE section. While

Allen et al. (1991) found no evidence of the Yalahe fault closer to Kangding city, most likely due to

the numerous villages in that valley hindering precise aerial mapping due to human modifications,

Liang et al. (2020) reported it from cross-sections at a few locations (Fig. 2B), where they found

312   that the active Yalahe fault cuts through gravel strata underneath radiocarbon-dated, early to mid-
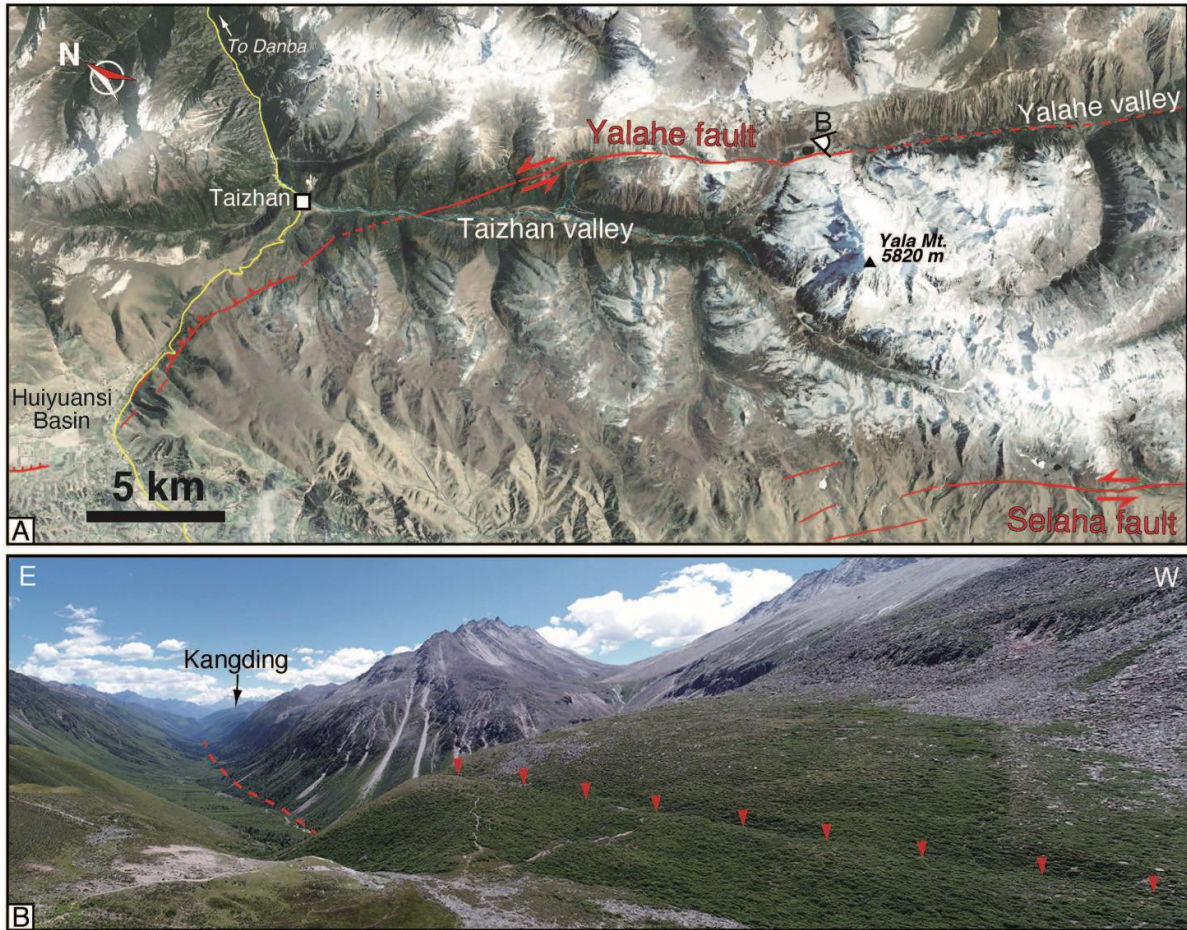
313   Holocene alluvial surfaces.

314

315

Figure 4: Yalahe fault. (A) Google Earth image of Yalahe fault between Huiyuansi Basin and Yalahe valley. Legend as in Figure 1. (B) View looking south along fault, with clear, linear, ~1 m-high scarp. Farther SE, fault trace becomes hard to follow (dashed line).

319

4.2. Selaha fault and Mugecuo pull-apart

321   While the Selaha fault was suggested as the main active branch of the SE XSH fault (Bai et

322   al., 2018), its trace between the Selaha pass and Mugecuo Lake is not as clear as that farther NW

323   and SE (Fig. 2B). To the NW, morphological evidence for active faulting abound along a linear

324   N144°E trend where the TG and SLH sites of Bai et al. (2018) are located (Fig. 2B), following the

325   geological fault that separates the Gongga-Zheduoshan batholith from Triassic sediments (Chen et

326   al., 1985) (Fig. 2C). It is along that fault that the Mw5.6 and Mw5.9 Kangding earthquakes occurred

327   in 2014. These earthquakes exhibit purely strike-slip focal mechanisms with a nodal plane striking

328   N139°-143°E for the first one and N148°-152°E for the second one (Jiang et al., 2015a), i.e.,

329   parallel to the NW Selaha fault (Fig. 2A). The fault left-laterally offsets the batholith's western edge

330   by ~15 km (Roger et al., 1995; Bai et al., 2018) (CC' in Fig. 2C). To the SE, the fault is continuous

331   and linear again, trending N154°, where Bai et al. (2018)'s YJG site is located (Fig. 5A). Between

332   these two linear fault splays, the strike of the Selaha fault is however N116°E for ~14 km, where

333   Mugecuo Lake is located. This segment probably has an important normal component and defines a

334   releasing bend (Allen et al., 1991; Bai et al., 2018). However, the precise geometry and individual

335   fault traces in that releasing bend were not clearly documented until now.

336   The ~600 m-high (Fig. 5F), steep topographic slope marking the north bank of Mugecuo

337   Lake (Yala Range) most likely corresponds to the morphological expression of a recent normal fault

338   trending N116°E and is cut by several topographic scarps that we interpret as secondary faults (Fig.

339   5A). South of the lake, the NE slopes of the Zheduoshan Range (NW part of Daxue Range) are less

340   steep but our UAV (Fig. 5C) and field (Fig. 5B,D,E) surveys revealed countless ~N110°-140°E-

341   trending topographic scarps up to ~10 m-high, in a ~22 km-long, ~3 km-wide, ~N120°E zone (Pan

342   et al., 2020). We interpret these scarps as the morphological expression of active normal faults

343   constituting the 'Mugecuo South fault zone' (Pan et al., 2020), which not only confirm that the

344   Mugecuo Lake area is a releasing bend between the two linear splays of the Selaha fault, but also

345   show that it is a 14x4.5 km-large pull-apart basin with Mugecuo Lake located at its lowest point

346   (Figs. 2B and 5A,F).

347   While Wen (2000) and Wen et al. (2008) inferred, following Li et al. (1997), that the M7.0

348   1725 earthquake produced ~35 km of surface ruptures along the SE Selaha fault, with maximum co-

349   seismic offsets of ~3.5 m, we however, infer that this earthquake may have occurred on the

350   Mugecuo South fault zone, which was unknown until now. This is partly due to the fresher nature of

351   the scarps with free-faces (dip >70°, Fig. 5B) at places along the Mugecuo South fault zone,

352   compared to those along the SE Selaha fault, although not as fresh as those from the 1955

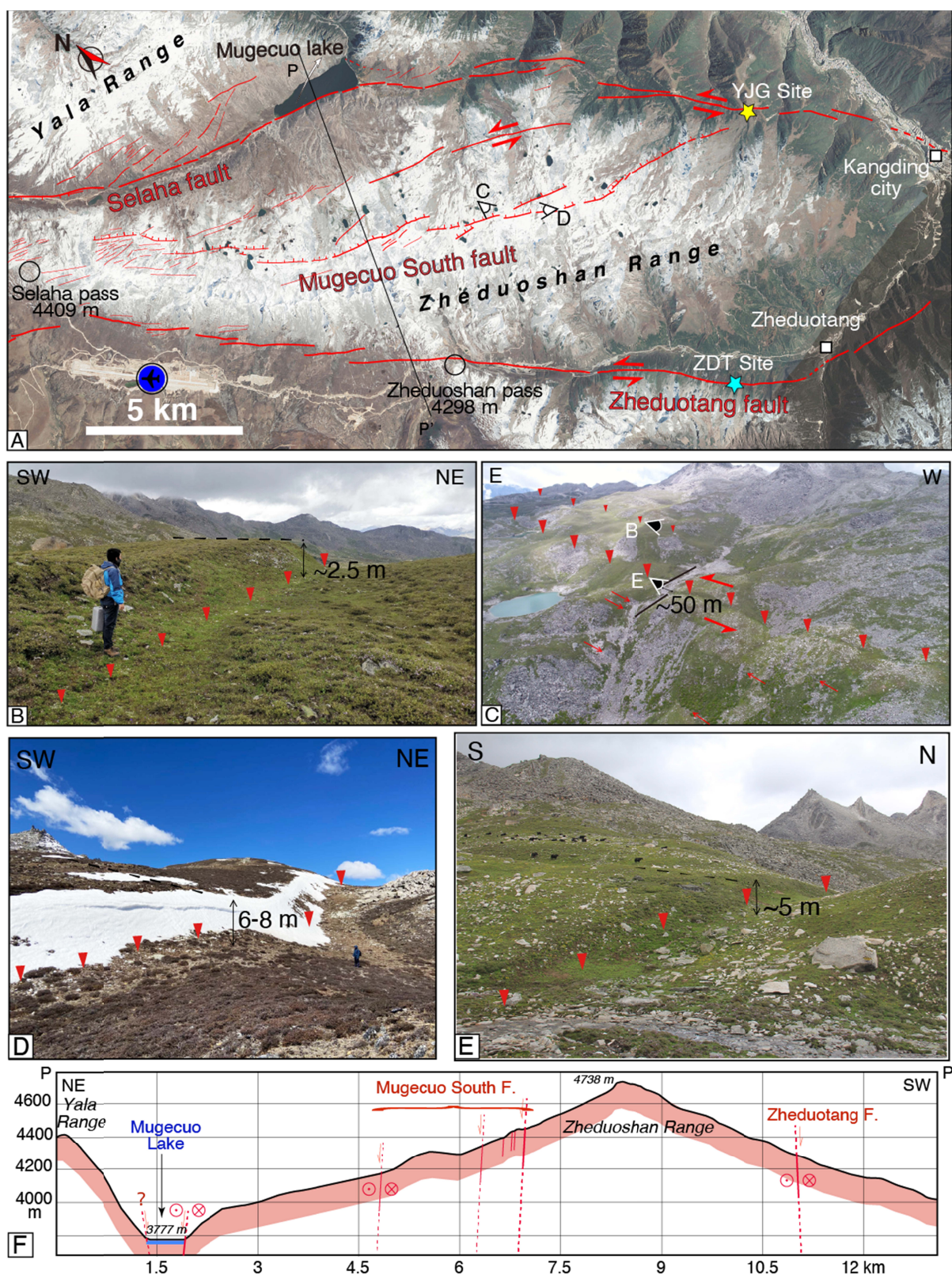353   earthquake that occurred along the Zheduotang fault.

354

355

Figure 5: *Mugecuo South fault zone and releasing bend. (A) Google Earth image of Selaha,*

Zheduotang and Mugecuo South faults between Selaha pass and Kangding. Legend as in Figures 1

and 2. (B,D,E) Field photos of fault scarps along Mugecuo South fault zone. (C) UAV photo of

faults from Mugecuo South fault zone highlighted by red triangles and arrows. Note left-lateral

offset. (F) Topographic profile across Mugecuo pull-apart and Zheduoshan Range (NW part of

Daxue Range). Recent faults in red, dashed where unknown.

362

4.3. Zheduotang fault and ZDT site

South of the Mugecuo pull-apart, the ~27 km-long, N148°-striking Zheduotang fault left-laterally offsets the western boundary of the Gongga-Zheduoshan batholith by ~10 km (Bai et al., 2018) (DD' in Fig. 2C). The fault follows the SW slopes of the Zheduoshan Range for ~13 km, from Kangding airport to the Zheduoshan pass, before becoming hard to follow in the valley due to the Kangding-Lhasa highway, until it reaches the mountain slopes on the other side of the valley (Fig. 5A). There, the Zheduotang fault sharply cuts about half-way for ~7 km, the NE-facing, steep (~35°), slopes on which numerous rockslides are present (Fig. 6A,B,D). It is along that section that the fault best displays left-lateral offsets of moraines (Fig. 6A,D). The fault has a slight normal component of motion with SW (uphill)-facing scarps, resulting in numerous sag ponds along the fault, particularly impressive along the section between the highway and Zheduotang village where the scarps can reach 8-10 m-high (Fig. 6B,C). That section ruptured during the 1955 Mw7.5 earthquake, that shows a purely left-lateral focal plane (N137°E, dip 89° to SW, obtained by recalibration of the initial motion directions of P waves recorded by 10 strong earthquakes along the XSH fault, Lin et al., 1986) that is roughly parallel to the fault trace (N148°E) (Fig. 2A). Farther to the SE, the Zheduotang fault changes direction to become ~N95°, reaches the valley again at Zheduotang village and cuts the mountain slopes for another ~2 km before it becomes hard to follow (Fig. 6A).

381

382
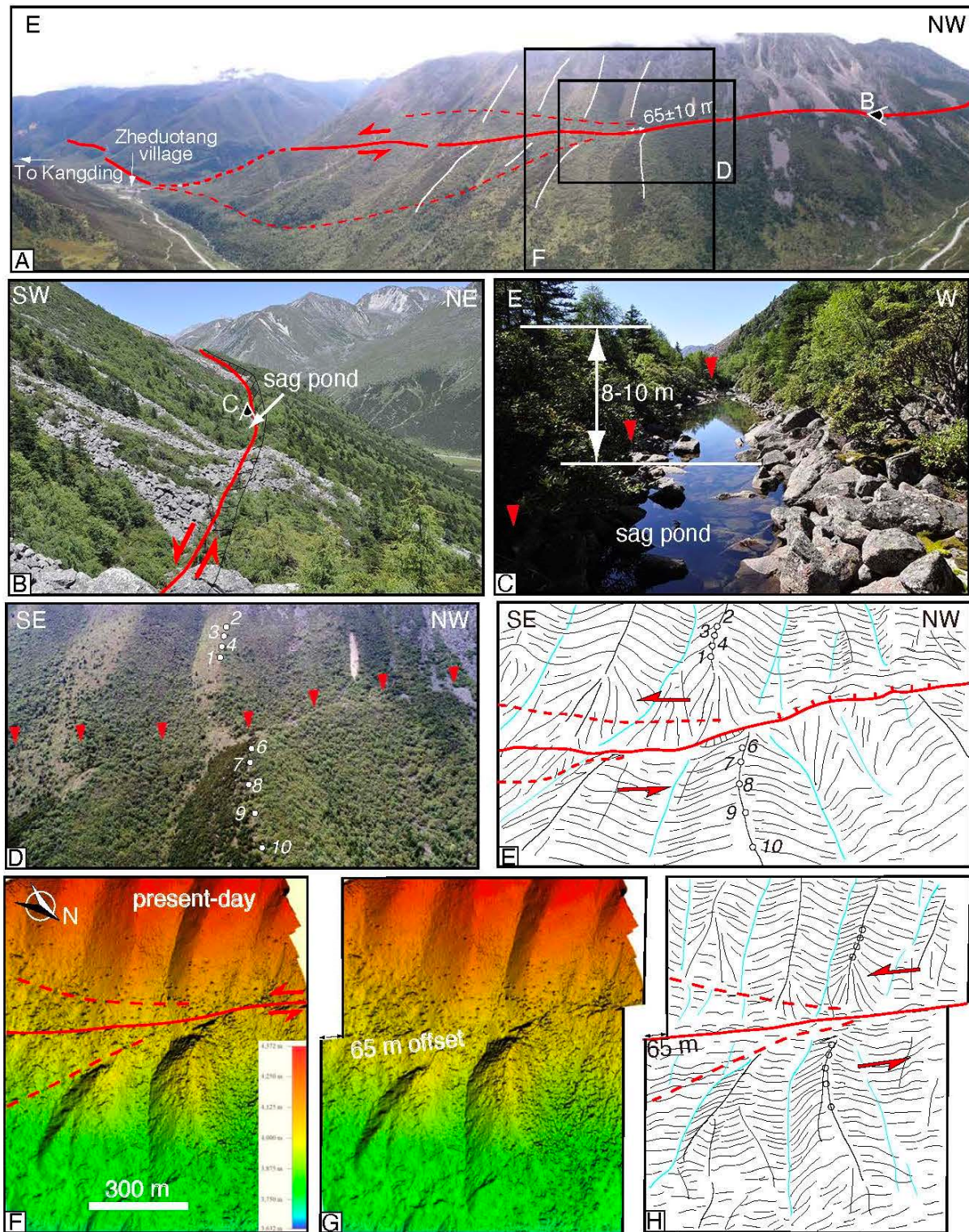
Figure 6: *Zheduotang fault and ZDT site. (A) Panoramic UAV photo of SE segment of Zheduotang*

fault with white lines highlighting offset moraine crests. (B) Photo of uphill-facing fault scarp along

which numerous sag ponds are present. (C) Photo of uphill-facing, 8-10 m-high, fault scarp. (D,E)

UAV photo of ZDT moraine with white circles and numbers representing collected samples (ZDT-1

387 *to 10) and its interpretation. (F,G) Present-day and offset reconstruction of 65±10 m offset on*

388 *LiDAR DEM obtained from our UAV surveys. (H) Interpretation of G.*

389

390   The remote Zheduotang (ZDT) moraines are located ~ 10 km due west of the city of

391 Kangding, at ~3860 m of elevation (Figs. 2B and 6). Their sub-rounded crests are ~1 km-long and

392 are covered with medium-sized granite boulders (~1 m of diameter) (Fig. S1). While the upper crest

393 is only covered with small bushes and occasional trees, the lower crest is covered with denser

394 vegetation, especially on its outer slope (Fig. 6D). The Zheduotang fault cuts and left-laterally

395 offsets the ZDT moraines by 65±10 m (Figs. 6F-H). The steep slopes, extremely dense vegetation at

396 lower elevations, numerous rockslides with very large, angular boulders, and the large stream at the

397 base of the mountain slopes (difficult to cross), all made this site extremely challenging to reach.

398 We eventually were able to collect a total of nine samples from the NW crest: five upstream from

399 the fault (ZDT-1-4) and five downstream (ZDT-6-10) (Fig. 6D). Ages range from 12.7±1.0 ka to

400 30.0±2.4 ka (Fig. 7 and Table 2). Applying statistical tests (see method section) allows to discard

401 the two oldest samples, with the remaining seven samples being well-clustered (moraine is Class

402 A), ranging from 12.7±1.0 to 15.9±1.2 ka. Therefore, the average age, 14.3±1.1 ka, is taken to

403 represent the moraine's abandonment age. Combining offset and age yields a left-lateral slip-rate of

404 4.5(+0.9/-0.8) mm/yr, or a range of slip rate between 3.7 and 5.4 mm/yr.

405

406
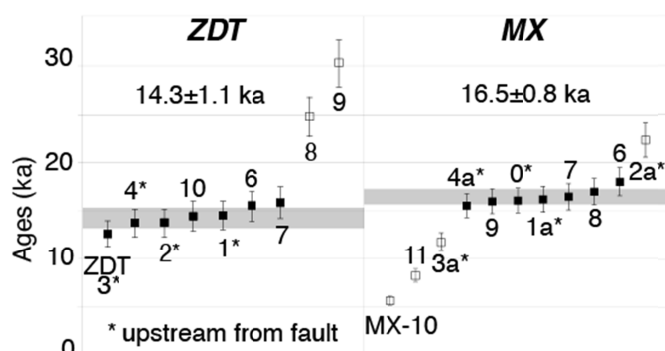
407 ***Figure 7:*** *[10]Be cosmogenic surface-exposure ages of ZDT and MX moraines, calculated using*
408 *CRONUS v3 (Balco et al., 2008), with 'Lm' production rate model (Lal (1991)/Stone (2000) time-*
409 *dependent model). Outliers (open symbols) were discarded using Chauvenet and Peirce criteria*
410 *(see method section for details).*

411

412 ***Table 2:*** *[10]Be surface-exposure ages of Zheduotang (ZDT) and Moxi (MX) sites of the SE*
413 *Xianshuihe fault.*

| Sample name	Lat (°N)	Long (°E)	Elev.	shielding	10Be(at/g)	Lm ages (yrs)	Int. Uncert.	LSDn ages (yrs)	Int. Uncert.
ZDT site									
upstream ZDT-1									
	30.007218	101.853394	3938	0.97	582604±9527	**14523±1132**	241	14815±922	246
ZDT-2	30.007075	101.852399	4024	0.97	569669±11427	**13748±1083**	280	13920±881	283
ZDT-3	30.007142	101.85266	3998	0.97	506680±9258	**12655±990**	234	12908±808	239
ZDT-4	30.007173	101.853023	3954	0.97	544843±12160	**13643±1083**	309	13863±888	314
downstream ZDT-6									
	30.008677	101.855455	3818	0.97	588013±11776	**15418±1217**	314	15771±1000	321
ZDT-7	30.00863	101.855689	3813	0.97	604810±11605	**15863±1249**	310	16259±1027	318
ZDT-8#	30.008681	101.856037	3831	0.97	1018291±17250	**24910±1968**	434	25226±1591	439
ZDT-9#	30.009041	101.856574	3796	0.97	1222029±15333	**30046±2360**	389	30494±1901	395
ZDT-10	30.00918	101.856736	3779	0.97	534327±9037	**14453±1129**	248	14817±924	255
Moxi site									
upstream MX-0									
	29.88182	102.009519	3877	0.99	644968±14438	**16099±1282**	373	16434±1056	382
MX-1a	29.881898	102.009739	3879	0.99	651371±19511	**16231±1334**	504	16556±1115	516
MX-2a#	29.881799	102.00999	3879	0.99	941220±19057	**22354±1779**	472	22654±1448	479
MX-3a#	29.881875	102.01018	3868	0.99	448416±10022	**11810±936**	273	12148±777	281
MX-4a	29.881813	102.010269	3870	0.99	620232±14033	**15559±1240**	365	15905±1022	374
downstream MX-6									
	29.883161	102.011295	3865	0.99	726534±15952	**18029±1437**	411	18470±1186	421
MX-7	29.883558	102.010804	3887	0.99	666039±21318	**16481±1368**	548	16866±1153	560
MX-8	29.880397	102.011228	3881	0.99	686869±13617	**17022±1345**	350	17392±1103	358
MX-9	29.882661	102.012665	3862	0.99	636352±12761	**16002±1264**	333	16361±1038	340
MX-10#	29.882107	102.0135603	3838	0.99	196027±6791	**5748±478**	204	6031±415	214
MX-11#	29.879169	102.016253	3777	0.99	290547±8810	**8329±680**	260	8714±584	273

414 Samples were processed at the Institute of Crustal Dynamics, China Earthquake Administration, Beijing (now called
415 National Institute of Natural Hazards, Ministry of Emergency Management of China), and the [10]Be/[9]Be ratios were
416 measured at GNS Science in New Zealand.
417 Ages are calculated with the CRONUS v3 calculator (Balco et al., 2008). Sample names with # represent outliers that

418   were statistically rejected (see text). All samples are granite (density 2.7 g/cm3); Shielding factor is 0.99 and 0.97 for
419   Moxi and ZDT sites, respectively. Thickness is 5 cm.

420   No erosion rate was applied. Standard used at GNS is '01-5-4', with $^{10}Be/^{9}Be$ = 2.851e-12.

421   Lm=Lal (1991)/Stone (2000) time-dependent production rate model; LSDn=Lifton et al. (2014) production rate model.

422

4.4. Moxi fault and MX site

424   The NNW-striking Moxi fault runs from Kangding to Moxi cities (Fig. 2B,C), lying between

425   the Proterozoic Kangding igneous complex and slivers of Paleozoic rocks (Lu et al., 1975; Liu et al.

426   1977). The fault shows evidence of recent faulting along its northern section where it cuts through

427   the western slopes of the Lamo-She Range, crosses the Yajiageng (or Xuemenkan) pass (3830 m)

428   then cuts through the eastern slopes of the Daxue Range (where Gongga Shan lies) (Fig. 8A). The

429   fault is very clear, with numerous offset moraines, gullies, and alluvial fans, forming sag ponds at

430   places thanks to its slight normal component of motion, with NE-facing scarps north of the pass and

431   SW-facing scarps to the south. While the main Moxi fault lies quite low on the mountain slopes,

432   numerous other fault strands are present higher on the slopes near the Yajiageng pass ('Moxi

433   rupture' in Fig. 8A,B) (Yan et al., 2019), with W to SW-facing scarps damming sag ponds. Farther

434   SE, the fault trace becomes harder to follow because it reaches the Moxi valley, which is filled with

435   large streams (coming directly from Gongga Shan), huge fluvio-glacial terraces and rockslide

436   deposits.

437

438
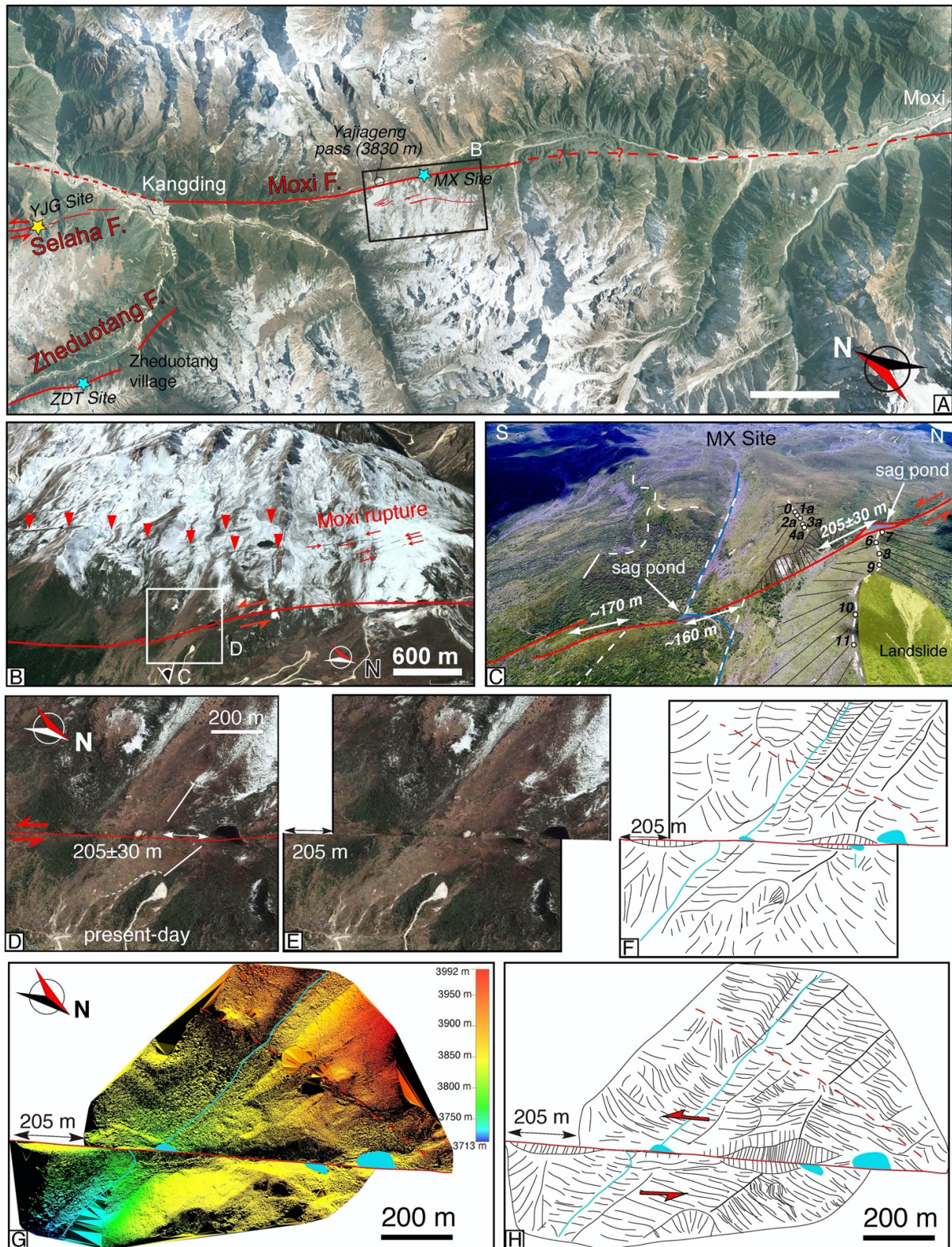
Figure 8: Moxi fault and MX site. (A) Google Earth image of Moxi, SE Zheduotang and Selaha
faults. Legend as in Figures 1 and 2. (B) Google Earth 3D image of Moxi surface ruptures parallel
to Moxi fault, located ~1 km to the west. (C) UAV photo interpretation of MX moraine. (D,E)

445

446   The ~1.5 km-long Moxi (MX) moraines are located along the segment just SE of the Yajiageng

447   pass, ~ 15 km SE of Kangding, at ~3850 m of elevation (Fig. 8). The MX moraine crests are sub-

448   rounded and covered with small bushes, and with medium granite boulders (Fig. S2). A landslide

449   removed part of the main moraine downstream from the fault (Fig. 8). Thanks to the left-lateral

450   motion on the Moxi fault, two sag ponds at the base of the resulting SW-facing scarps formed,

451   larger at the base of the northern crest (north of the stream, Fig. 8). The main northern and southern

452   (i.e., south of the stream) MX moraine crests are left-laterally offset by 205±30 and ~170 m,

453   respectively (Fig. 8). A smaller offset for the southern crest is excepted due to the sense of motion

454   of the Moxi fault, with the stream in between, whose offset is ~160 m at present, constantly

455   refreshing the lateral slopes.

456   We collected 11 samples at the MX site along the northern crests, five upstream from the

457   fault (MX-0, MX-1a-4a) and six downstream (MX-6-11) (Fig. 8C). Ages range from 5.7±0.5 to

458   22.3±1.8 ka (Fig. 7 and Table 2). Applying statistical tests allows to discard the three youngest and

459   the oldest samples. It is interesting to note that the young outliers are located the farthest

460   downstream, most likely reflecting material removal due to the landslide, which has reshaped the

461   crest to its present-day geometry. The original crest may thus only be preserved close to the fault,

462   where samples MX-6 to 9 are located. The seven remaining samples cluster very well and the

463   moraine is Class A. Therefore, the average age is taken to best represent the moraine's abandonment

464   age, which is 16.5±0.8 ka. Combining the offset and the age of the main, northern moraine yields a

465   left-lateral slip-rate of 12.5(+2.3/-2.1) mm/yr, or a range of 10.4 to 14.8 mm/yr. Note that the 'Moxi

466   rupture' (located ~1 km west of the Moxi fault, Fig. 8B) may also absorb part of the deformation,

467   thus the slip rate we determined is a minimum.

468

5. Discussion

5.1. Late Quaternary slip distribution across the various segments of the SE Xianshuihe fault

471   Along the NW XSH fault, where the single fault trace is linear and continuous, late

472   Quaternary left-lateral slip rates have been estimated at 8 - 11 mm/yr (#13a, Fig. 3 and Table 1)

473   (Zhang, 2013, reinterpreting Chen et al. (2008)'s data) and ~8.4 mm/yr (#14) (Liang et al., 2020).

474   From the Huiyuansi Basin, where the XSH fault splits into the Yalahe, Selaha, Mugecuo South and

475   Zheduotang branches, Bai et al. (2018), using the same technique as in this paper, determined rates

476   of 9.6-9.9 (TG+SLH sites, Fig. 3B) and 3.9 - 4.9 mm/yr (YJG site) along the NW and SE parts of

477   the Selaha fault, respectively, since ~20 ka. Our present study at the ZDT site allowed us to

478   determine a late Quaternary (~15 ka) rate of 3.7 - 5.4 mm/yr along the Zheduotang fault. Summing

479   the slip rates along the SE Selaha fault (YJG site) and the Zheduotang fault (ZDT site) yields 7.6-

480   10.3 mm/yr (ZDT+YJG, Fig. 3). This appears to confirm the inference of Bai et al. (2018) that

481   recent motion on the NW Selaha fault is then partitioned between the SE Selaha and the parallel

482   Zheduotang faults farther to the SE. However, the total XSH fault slip rate at this longitude should

483   also consider that along the Yalahe fault although it has been estimated to be quite low, and only

484   from its NW part where its normal component is important (Figs. 2B and 4A). It was first

485   qualitatively inferred as ~0.8 mm/yr (#12b, Fig. 3 and Table 1) (Allen et al., 1991), before being

486   constrained at 1.8 - 2.2 mm/yr over 10 ka (#20a) (Zhou et al., 2001) and 0.6 (over 10-15 ka) - 1.5

487   (over 70 ka) mm/yr (#21a) (Chen et al., 2016) from thermoluminescence ages. Therefore, assuming

488   similar rates along the SE Yalahe fault (0.6-2.2 mm/yr), in the absence of reported quantitative

489   measurements, the total late Quaternary slip rate across the Yalahe, SE Selaha and Zheduotang

490   branches becomes >8.2-12.5 mm/yr. Note that this rate is a minimum because the rate along the

491   Mugecuo South fault is currently unknown.

492   Along the Moxi fault, we determined a slip rate of 10.4 - 14.8 mm/yr since ~16 ka at the MX

493 site. Previously published rates (Zhou et al., 2001; Chen et al., 2016; Yan et al., 2017) range from

494 8.3 to 10.5 mm/yr at the northern extremity of the fault (Fig. 3 and Table 1). These three studies

495 used ^{14}C dating mostly in trenches dug across the fault, a method that is not the most accurate for

496 determining slip rates along strike-slip faults because horizontal offsets are difficult to measure in

497 trenches. Considering that all measurements are valid and assuming a constant rate along the fault

498 would imply a rate of ~10.4 mm/yr along the entire Moxi fault.

499   From NW to SE, the late Quaternary slip rates along the XSH fault system thus appear to

500 increase progressively from ~6-8 mm/yr along the Ganzi fault (Chevalier et al., 2017), ~8 - 11

501 mm/yr along the single-stranded NW XSH fault (Zhang, 2013, Liang et al., 2020), >8.2-12.5 mm/yr

502 across the Yalahe / Selaha / Mugecuo / Zheduotang segment (e.g., Bai et al., 2018, this study), to

503 10.4-14.8 mm/yr along the Moxi segment (Figs. 3B,C and 9).

504

5.2 Comparison with geodetic rates

506   Comparison between our late Quaternary rates and geodetic ones is not straightforward, in

507 part due to the still limited number of regional GPS stations north of the XSH fault. The two latest

508 publications based on GPS data have adopted different strategies.

509   On one hand, Wang et al. (2020) propose an elastic block model (Meade and Loveless,

510 2009) for SE Tibet that explains well the ~15 years-long dataset (Wang et al., 2017), especially

511 north of the Red River fault. They further discuss the along- and across-strike slip rates of the faults

512 in their model. They infer a 11.8±0.6 mm/yr slip rate along the Ganzi fault, that increases to

513 14.5±0.9 mm/yr (#10b in Fig. 3 and Table 1) along the XSH fault. The late Quaternary rates that we

514 propose (6–8 mm/yr for the Ganzi fault and >8.2 - 12.5 mm/yr for the SE XSH fault) represent

515 ~70% of these rates. This difference may be explained by the fact that the block model considers

516 that all deformation between the blocks is absorbed along the bounding faults while in fact, a

517 fraction of the deformation may also be absorbed by other smaller structures within the blocks.

518 On the other hand, Wang and Shen (2020) propose a GPS-derived deformation field for most

519 of continental China based on a ~15 years-long dataset. They consider that in Tibet, including in the

520 XSH fault region, deformation is mostly continuous and cannot be described by the relative motion

521 of minimally-deformed blocks. In that case, deformation is instead quantified along velocity

522 profiles. In order to see a clear trend in the rate evolution on both sides of the fault, it is wise to

523 make wide (~100 km) and long (>300 km) transects perpendicular to the fault, however not

524 specifically targeted to the particular study of the XSH fault. Profiles from Wang and Shen (2020)

525 show a slight increase of velocity from ~11 mm/yr across the Yalahe/Selaha faults (section A-A' in

526 Fig. 9A,B, #24a in Fig. 3 and Table 1), to ~13 mm/yr across the Moxi fault (section B-B', #24b).

527 While the limit between their sections AA' and BB' falls near the Selaha pass, these GPS estimates

528 are still consistent with what we determined at the late Quaternary timescale across faults from both

529 sections.

530 The most recent GPS datasets, analyzed in two different ways, both suggest a progressive

531 increase toward the SE of the left-lateral slip rate along the XSH fault, as we document in this study

532 at a much longer timescale. Similarly, the most recent InSAR study (Qiao and Zhou, 2021) suggests

533 an increase from 8.1 - 11.1 mm/yr along the NW XSH fault (#7b in Fig. 3 and Table 1), to 8.8 - 16

534 mm/yr across the SE XSH fault (#7c), and 16.5 - 19.3 mm/yr along the Moxi fault (#7d). Note

535 however that the authors invoke possible overestimate of the latter due to unwrapping and local

536 atmospheric errors. A SE rate increase until at least Moxi would be in agreement with the observed

537 eastward projected rate decrease observed from GPS vectors relative to stable Eurasia located north

538 of the XSH fault system, from the Bayan Har block to the Longmenshan block, as well as from the

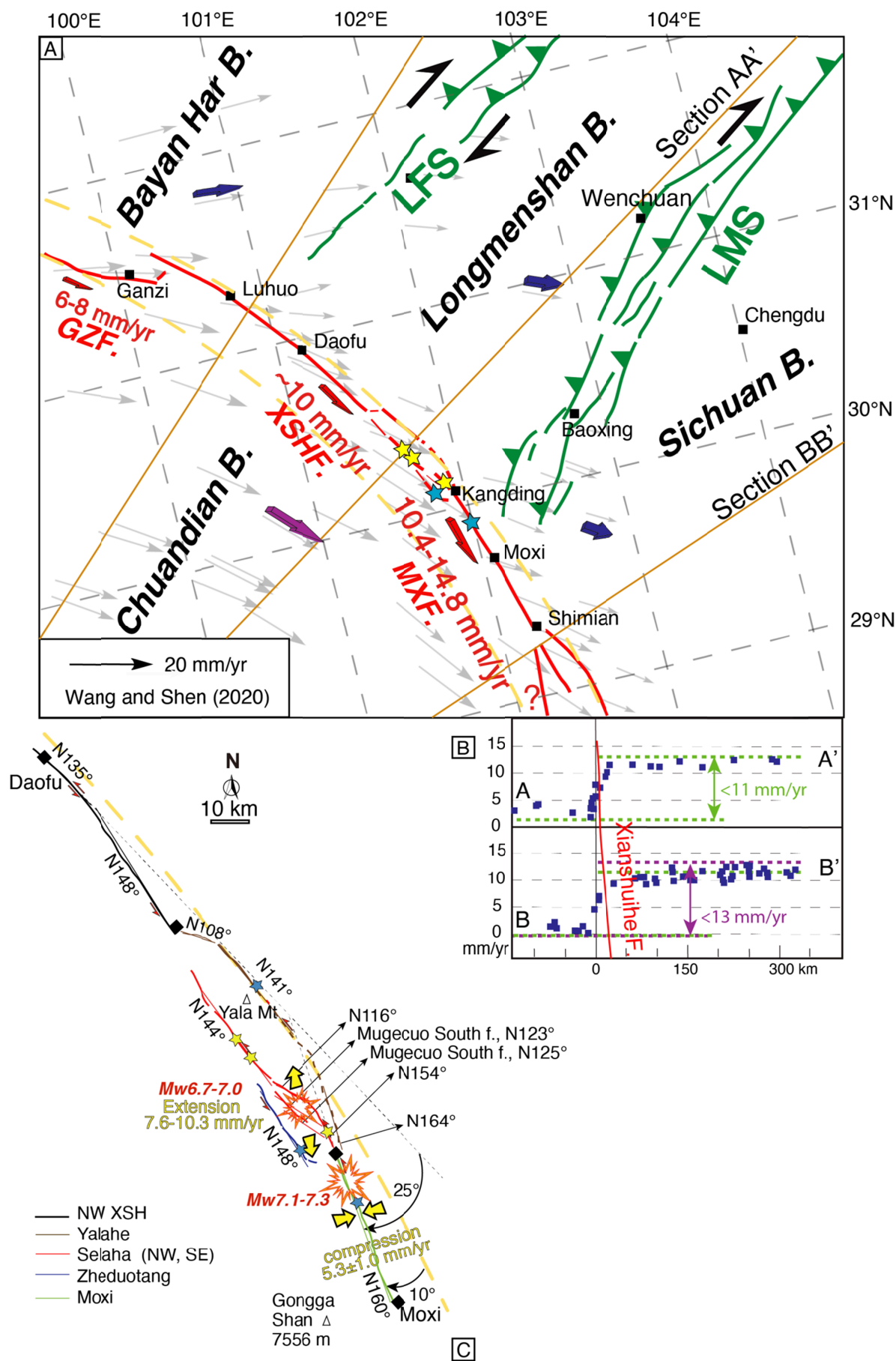539 Longmenshan block to the Sichuan Basin (Fig. 9A).

540

542 **Figure 9:** *(A) Conceptual 2D model of Xianshuihe fault following India–Asia collision (modified*
543 *from Bai et al., 2018). Red arrows show southeastward slip rate increase, with rates from Chevalier*
544 *et al. (2017) along the Ganzi fault (GZF), Bai et al. (2018) (yellow stars) along Xianshuihe/Selaha*
545 *fault (XSHF), and this study along Moxi fault (MXF) (light blue stars). LFS=Longriba fault system,*
546 *LMS=Longmenshan. Orange dashed lines show small circles (with pole of rotation in eastern*
547 *Himalayan syntaxis) that fit with trace of Xianshuihe fault system. Grey arrows show GPS vectors*
548 *relative to stable Eurasia (Wang and Shen, 2020) with oblique orange lines representing extent of*
549 *their fan-shaped sections AA' and BB' shown in (B). Blue and pink arrows show block movement on*
550 *each side of Xianshuihe fault system with their appropriate lengths according to GPS velocities. (B)*
551 *Tangential (sinistral positive) components of GPS velocity profiles modified from Wang and Shen*
552 *(2020) (with respect to Eurasia) with maximum rate across Xianshuihe and Moxi faults in green*
553 *and pink, respectively. This is consistent with the increase in slip rate between the two fault*
554 *segments we suggest with our late Quaternary rates. (C) Fault traces (thick colored lines) and*
555 *strike directions (thin colored lines) of Xianshuihe fault. Dashed black lines show ~25°clockwise*
556 *bend between NW XSH and Moxi fault segments. Yellow arrows represent directions of extension*
557 *(Mugecuo pull-apart basin and compression (Moxi fault). Earthquake hazard (and their estimated*
558 *magnitude in red) is indicated by large orange stars (see discussion in text).*

559

5.3 Example of a pull-apart basin within a restraining bend

561   While the NW XSH fault has a single, linear and continuous trace striking N135°E for ~180

562 km, its geometry changes dramatically near the Huiyuansi Basin (N148°E), where it splits into the

563 four en-echelon faults discussed here (Yalahe-Selaha-Mugecuo-Zheduotang), before resuming as a

564 single fault trace striking N160°E (Moxi segment) (Figs. 2 and 9C). This ~25° clockwise bend has

565 been interpreted to have formed a restraining bend that would explain the very high elevations of

566 the Yala (peak at 5820 m) and Daxue (Gongga Shan peak at 7556 m) Ranges (Allen et al., 1991;

567 Burchfiel et al., 1995; Zhang et al., 2017). Zhang et al. (2017) interpreted the onset of rapid

568 exhumation (at a rate of ~1.85 mm/yr) of the Yala Range at ~9 Ma, as corresponding to the

569 restraining bend initiation, and thus, to the propagation of the XSH fault first along the Yalahe fault.

570 They then interpreted the exhumation rate decrease at ~4 Ma in the Yala Range, as due to slip rate

571   decrease along the Yalahe fault, and further activation of the Selaha and Zheduotang faults. This

572   resulted in a southward shift in the restraining bend from the Yala to the Daxue Range, where the

573   highest peaks are now located.

574   This mountain range indeed shows the fastest present-day erosion rates in the entire eastern

575   margin of the Tibetan Plateau, between 1.0±0.4 and 7.6±2.5 mm/yr, derived from ^{10}Be

576   concentrations in river sand (Ouimet et al., 2009; Cook et al., 2018) (orange contour in Fig. 2C).

577   Cook et al. (2018) estimated that such very fast localized exhumation (at rates of ~3 mm/yr) lasts

578   since 3–4 Ma. While this timing is consistent with that proposed by Zhang et al. (2017) using

579   thermochronology dating, Cook et al. (2018) suggested that the geometry of the restraining bend

580   can only account for a fraction of the fast exhumation rate. Indeed, considering that motion is purely

581   strike-slip along the XSH fault, a ~12.5 mm/yr (or 10.4-14.8 mm/yr) of left-lateral slip along the

582   Moxi segment (this study) in a 25° restraining bend (angle between the XSH and Moxi segments)

583   would imply a 5.3±1.0 mm/yr compression across the Moxi segment in a planar geometry (Fig.

584   9C). Such compression may potentially explain the high exhumation rates in the Daxue Range

585   (Cook et al., 2018). However, the entire XSH fault system appears to follow a small circle

586   corresponding to a Euler rotation pole located in the Eastern Himalayan Syntaxis (25.0829°N -

587   93.5747°E in Bai et al., 2018, Fig. 10A; 25.65°N - 94.31°E in Cook et al., 2018). Considering that

588   small circle as representing a direction of pure strike-slip motion, the bend then becomes ~10° (Fig.

589   9C), which would imply only 2.2±0.4 mm/yr of compression across the Moxi fault, an amount too

590   small to solely explain the fast present-day exhumation rates in the Daxue Range (Cook et al.,

591   2018). Sixty kilometers to the south, the Moxi fault splits into the Anninghe and Daliangshan faults

592   that left-laterally offset the Yangtze River by ~60 km (Wang et al., 1998) (near ~27°N, Fig. 1). The

593   northern Anninghe fault striking N185°E implies another ~25° of clockwise rotation of the direction

594   of motion, hence another restraining bend (Fig. 1). However, that bend is located too far south to

595   explain the high erosion and very high elevations in the Gongga Shan region (Cook et al., 2018).

596   Therefore, in this tectonic setting, subsidence in the Mugecuo area (Fig. 5A) is rather

597   surprising in a zone of high elevations and recent fast exhumation rates. The geometry of the SE

598   Selaha and Zheduotang faults is typical of a large-scale (~4.5 km-wide) pull-apart basin (Fig. 5A) in

599   between the Yala Range, where fast exhumation occurred between 9 and 4 Ma (Zhang et al., 2017),

600   and the Daxue Range, where very fast exhumation occurs since ~4 Ma (Cook et al., 2018). Local

601   subsidence thus appears to be the consequence of strike-slip motion on the SE Selaha fault striking

602   N154° and the Zheduotang fault striking N148° (Figs. 9C and 10). The corresponding amount of

603   NW-SE extension within the Mugecuo pull-apart basin can thus be estimated by summing the rates

604   along these two bounding faults: 3.9 – 4.9 mm/yr for the SE Selaha fault at the YJG site (Bai et al.,

605   2018) and 3.7 - 5.4 mm/yr for the Zheduotang fault at the ZDT site (this study), thus a total of 7.6 –

606   10.3 mm/yr (Figs. 9C and 10). This value would correspond to that of the subsidence in the pull-

607   apart basin if every fault strand was vertical, and would thus yield an upper bound for the total

608   vertical motion.

609   At such rate, the ~600 m-deep Mugecuo Lake depression (Fig. 5F) would form in 60 to 80

610   kyrs. This only represents a first order estimate as it does not account for erosion nor the actual dip

611   of the faults (which remains to be constrained). While these variables would both increase the pull-

612   apart's duration of formation, it is nevertheless compatible with the ages of the regional offset

613   landforms (e.g., Chevalier and Replumaz, 2019). In addition, in the pull-apart basin, vertical motion

614   appears asymmetrical, with a ~300 m higher topography and more numerous normal fault strands

615   on the SW side compared to that on the NE (Fig. 5F). This is consistent with much faster

616   exhumation rates (determined from cosmogenic [10]Be basin-wide measurements) to the SW

617   compared to the NE (Fig. 2C) (Ouimet et al., 2009; Cook et al., 2018). However, the zone of fastest

618   exhumation is located ~30 km farther south (Cook et al., 2018) (Fig. 2C) and cannot be explained

619   by the pull-apart kinematics alone. We thus interpret the Mugecuo zone as a pull-apart basin within

620   a larger restraining bend (see discussion above), which implies a complex 3D fault geometry (Fig.

621   10) that has, to our knowledge, rarely been described.

622   A striking peculiarity of the Yalahe-Selaha-Mugecuo-Zheduotang segments is that they are

623   located where the XSH fault crosscuts a ~120 km-long granite batholith that formed during at least

624   four distinct magmatic episodes (obtained from U/Pb zircon ages): Triassic (Gongga granite, 216-

625   204 Ma), Middle Jurassic (Zheduo granite, ~170 Ma), Oligocene (~27 Ma) and Miocene (20-13

626   Ma) (Roger at al., 1995; Li and Zhang, 2013; Li et al., 2015; Searle et al., 2016). This batholith is

627   the only Cenozoic massif in all of SE Tibet, and crystallization ages as young as ~5 Ma have been

628   reported (Searle et al., 2016; Zhang et al., 2017). Ar/Ar ages are as young as 3.5 Ma (Wallis et al.,

629   2003; Zhang et al., 2004; Chen et al., 2006) and apatite fission track ages are as young as 1.2 Ma

630   (Xu and Kamp, 2000; Wilson et al., 2011; Zhang et al., 2017). Such very young ages imply a high

631   geothermal gradient that may be one of the contributing factors to the present-day fast exhumation

632   rates (Cook et al., 2018). Indeed, young magmatism and high heat flow may favor uplift. However,

633   young (≤5 Ma) granite bodies are rare and small in extent, so that it is challenging to quantify this

634   possible effect.

635   It is also surprising that the local trace of the faults at the surface is so complex where it

636   crosses the granite batholith, which is most likely more rigid than the surrounding Triassic flysh.

637   Indeed, farther north, where the Ganzi segment of the XSH fault system cuts and offsets the

638   Mesozoic Queer Shan granite by 76–90 km (Wang and Burchfiel, 2000; Wang et al., 2009), the fault

639   trace is linear and does not appear to be affected by lithology (Fig. 1). Therefore, the key point may

640   thus be that the young age of the granite and/or the high regional flow concur to create the high

641   elevation of Gongga Shan, in addition to the precipitation that possibly pre-existed along the SE

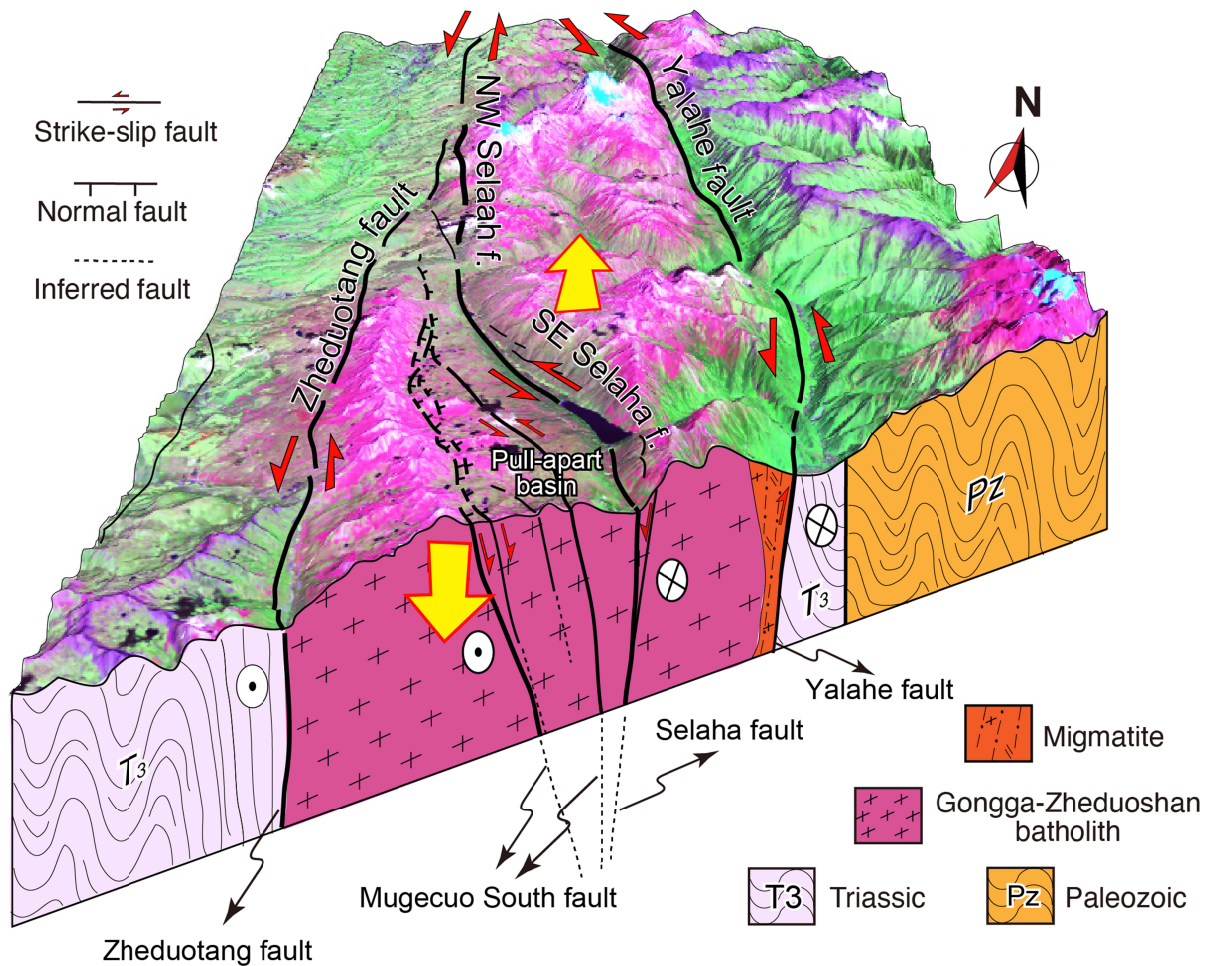642   Tibetan Plateau margin due to the topographic step (Cook et al., 2018).

643

Figure 10: *3D geomorphic model of Mugecuo South fault zone area (mostly normal, with minor left-lateral motion), which forms a large-scale pull-apart basin with Mugecuo Lake in its lowest point. Legend as in Figure 2. Top image is Landsat.*

5.4 Seismic hazard in the Kangding region

Using the late Quaternary slip rates we determined in this study helps us calculate the current slip deficit since the last large earthquake occurred along a particular fault segment using empirical equations from Wells and Coppersmith (1994). Satellite images analysis and field investigation confirmed that at least the NW and central segments of the Yalahe fault are active with recent, as well as cumulative, offsets, while the potential activity along the SE part remains to be assessed. Taking a 0.6 - 2.2 mm/yr rate (as suggested for the NW part), a slip deficit of only 19 - 70

656   cm would have accumulated since the last large earthquake in 1700 (M7). This would correspond to

657   a Mw6.2 - 6.6 earthquake hazard at present (Wells and Coppersmith, 1994:

658   M=6.69+0.74*log[maximum displacement of 0.19 - 0.7 m]).

659   The Kangding region of the SE XSH fault is regarded as a seismic gap, partly because of the

660   regional Coulomb stress increase following the 2008 Wenchuan (e.g., Parsons et al., 2008; Toda et

661   al., 2008; Shan et al., 2009; Nalbant and McCloskey, 2011) and 2013 Lushan (Ms7.0) (Shan et al.,

662   2013; Yang et al., 2015; Guo et al., 2018) earthquakes, and in part because the energy accumulated

663   in the region since the 1955 Mw7.5 Kangding earthquake was only partly released during the 2014

664   Mw5.9 and 5.6 Kangding earthquake sequence (e.g., Jiang et al., 2015a; Xie et al., 2017). Based on

665   the coulomb stress evolution of co-seismic dislocation and post-seismic viscoelastic relaxation, and

666   on time-dependent probabilistic risk models, the Bamei-Selaha-Kangding segments in particular

667   have been shown to have a high earthquake probability in the near future (e.g., Xu et al., 2013,

668   2019; Shao et al., 2016). Geophysical studies also indicate a high seismic hazard in that region (e.g.,

669   Jiang et al., 2015a; Wang and Shen, 2020).

670   At a more detailed level, the Selaha fault has especially been suggested as a seismic gap

671   because of the absence of large earthquakes since 1748 along its NW section, and 1725 along its SE

672   section, respectively, with a M~7 earthquake risk at present (e.g., Allen et al., 1991; Wen, 2000;

673   Wen et al., 2008; Papadimitriou et al., 2004; Cheng et al., 2011; Shao et al., 2016; Bai et al., 2018;

674   Qiao and Zhou, 2021). However, our discovery of the Mugecuo South fault zone followed by our

675   recent field investigation, revealed numerous normal fault strands with cumulative fault scarps up to

676   ~10 m-high at places (Pan et al., 2020). Although the geometry of the fault is different from that of

677   the more linear and continuous traces of the Yalahe and Zheduotang faults, the numerous fault

678   strands at the surface may connect at depth. Because the Selaha and Mugecuo South faults together

679   form a large-scale pull-apart basin bounded by numerous normal fault strands, the pull-apart may

680   lose stability more easily and rupture through (Segall and Pollard, 1980; Li et al., 2015). We thus

681   suggest that large earthquakes may more easily occur in that zone of the Mugecuo pull-apart basin,

682   compared to other sections of the Selaha fault. As the slip rate along the Mugecuo South fault is still

683   unknown, taking that of the NW or SE Selaha fault (~9.75 and 3.9 - 4.9 mm/yr, respectively), would

684   yield a slip deficit of ~2.8 or 1.2-1.5 m, respectively since 1725. This would correspond to a

685   potential earthquake as high as ~Mw6.7 - 7.0 at present (M=6.69+0.74*log[maximum displacement

686   of 2.8 m], Wells and Coppersmith, 1994).

687   Similarly, taking our 10.4 - 14.8 mm/yr rate along the Moxi fault would correspond to a slip

688   deficit of 2.4 - 3.5 m since the last large (M7.75) earthquake in 1786, i.e., a potential earthquake of

689   Mw7.1-7.3 at present, consistent with what Qiao and Zhou (2021) determined (Mw7.37) using an

690   elastic dislocation model. These authors also determined that the return time of characteristic large

691   earthquakes (Mw7.25) along the Moxi fault is 155 years. The fact that the last large earthquake

692   occurred 235 years ago may thus suggest that an earthquake is overdue along that segment hence a

693   high seismic risk. This would devastate Moxi town, which, despite currently being less populated

694   than Kangding city, continuously expands to cater to increasing tourism, thanks to its location at the

695   base of Gongga Shan.

696

697   **6. Conclusion**

698   By studying four locations along the four en-echelon faults of the SE Xianshuihe fault:

699   (1) We quantitatively determined that the late Quaternary slip rate along the Zheduotang fault is 3.7

700   - 5.4 mm/yr.

701   (2) We discovered a new fault zone (Mugecuo South) between the SE Selaha and Zheduotang

702   faults, along which numerous, mostly normal, fault strands with cumulative scarps up to ~10 m

703   exist. Due to the fresh nature of the scarps, we infer that the 1725 M7.0 earthquake may have

704   occurred along that particular fault zone. This new fault segment forms a large-scale pull-apart

705   basin causing subsidence of the Mugecuo Lake zone.

706   (3) The Mugecuo pull-apart basin is located in a zone of exceptionally high elevation (visible as

707   highest peak Gongga Shan, 7556 m) due to the large-scale restraining bend along the Xianshuihe

708   fault, possibly in conjunction with high heat flow and intense erosion.

709   (4) We suggest from field investigation, that the central part of the Yalahe fault is active, with clear

710   fault scarps that can be followed for ~10 km. While slip rates are still lacking, we suggest that it

711   most likely also contributes to the total slip rate of the SE Xianshuihe fault.

712   (5) We determined that SE of Kangding, the late Quaternary slip rate along the Moxi fault ranges

713   from 10.4 to 14.8 mm/yr.

714   (6) The slip rate along the Xianshuihe fault system thus increases to the SE from 6-8 mm/yr along

715   the Ganzi fault, to 8-11 mm/yr along the NW Xianshuihe fault, to 8.2-12.5 mm/yr along the SE

716   Xianshuihe fault, to 10.4-14.8 mm/yr along the Moxi fault.

717   (7) We suggest that high seismic hazard exists in the SE Xianshuihe fault, especially in the

718   Mugecuo pull-apart basin, which may facilitate earthquakes nucleation.

719

727

References

Allen, C.R., Luo, Z., Qian, H., Wen X., Zhou, H., & Huang, W. (1991). Field study of a highly active fault zone: The XSF of southwestern China. *Geological Society of America Bulletin, 103*, 1178–1199. Doi:10.1130/0016-7606(1991)103<1178:FSOAHA>2.3.CO;2

Bai, M., Chevalier, M.L., Pan, J., Replumaz, A., Leloup, P.H., Métois, M., & Li, H. (2018). Southeastward increase of the late Quaternary slip-rate of the Xianshuihe fault, eastern Tibet. Geodynamic and seismic hazard implications. *Earth and Planetary Science Letters, 485,* 19-31. Doi:10.1016/j.epsl.2017.12.045

Balco, G., Stone, J.O., Lifton, N. A., & Dunai, T.J. (2008). A complete and easily accessible means of calculating surface exposure ages or erosion rates from ^{10}Be and ^{26}Al measurements. *Quaternary Geochronology, 3*, 174-195. Doi:10.1016/j.quageo.2007.12.001

Bevington, P.R., & Robinson, D.K. (2002). Data reduction and error analysis for the physical sciences. 336pp, McGraw-Hill

Burchfiel, B.C., Chen, Z., Liu, Y., & Royden, L.H. (1995). Tectonics of the Longmen Shan and adjacent regions. *International Geology Review, 37*, 661–736

Chen, W., Tan, Q., Wen, P., & Liang, X. (1985). Geological map of Kangding (H-47-18). Sichuan Institute of Geology and Mineral Resources, Scale 1/200,000

Chen, W., Zhang, Y., Zhang, Y.Q., Jin, G.S., & Wang, Q.L. (2006). Late Cenozoic episodic uplifting in southeastern part of the Tibetan plateau-evidence from Ar–Ar thermochronology. *Acta Geologica Sinica, 22,* 867–872. Doi:10.3969/j.issn.1000-0569.2006.04.010 (in Chinese)

Chen, G., Xu, X., Wen, X., & Wang, Y. (2008). Kinematical transformation and slip partitioning of northern to eastern active boundary belt of Sichuan-Yunnan block. *Seismology and Geology, 30*, 58-85 (in Chinese)

751   Chen, G., Xu, X., Wen, X., & Chen, Y. (2016). Late Quaternary slip-rates and slip-partitioning on

752   the southeastern Xianshuihe fault system, Eastern Tibetan Plateau. *Acta Geologica Sinica, 90*,

753   537-554. Doi:10.1111/1755-6724.12689

754   Cheng, J., Liu, J., Gan, W., Yu, H., & Li, G. (2011). Characteristics of strong earthquake evolution

755   around the eastern boundary faults of the Sichuan-Yunnan rhombic block. *Science China–*

756   *Earth Sciences, 54*, 1716–1729. Doi:10.1007/s11430-011-4290-2

757   Chevalier, M.L., Ryerson, F.J., Tapponnier, P., Finkel, R., Van der Woerd, J., Li, H., & Liu, Q.

758   (2005). Slip-rate measurements on the Karakorum fault may imply secular variations in fault

759   motion. *Science, 307(5708)*, 411–414. Doi: 10.1126/science.1105466

760   Chevalier, M.L., Hilley, G., Tapponnier, P., Van Der Woerd, J., Liu-Zeng, J., Finkel, R.C., Ryerson,

761   F.J., Li, H., & Liu, X. (2011). Constraints on the late Quaternary glaciations in Tibet from

762   cosmogenic exposure ages of moraine surfaces. *Quaternary Science Reviews, 30*, 528–554.

763   Doi:10.1016/j.quascirev.2010.11.005

764   Chevalier, M.L., Leloup, P.H., Replumaz, A., Pan, J., Metois, M., & Li, H. (2017). Temporally

765   constant slip-rate along the Ganzi fault, NW Xianshuihe fault system, eastern Tibet.

766   *Geological Society of America Bulletin, 130(3/4),* 396–410. Doi:10.1130/B31691.1

767   Chevalier, M. L., & Replumaz, A. (2019). Bimodal climatic signal for glaciations in SE Tibet:

768   Marine Isotope Stages 2 and 6. *Earth and Planetary Science Letters, 507*, 105-118.

769   Doi:10.1016/j.epsl.2018.11.033

770   CEA: China Earthquake Administration, Earthquake Disaster Prevention Department. Catalogue of

771   strong earthquakes in Chinese history. *Beijing Seismological Press*, 1995.

772   Cook, K.L., Hovius, N., Wittmann, H., Heimsath, A.M., & Lee, Y. (2018). Causes of rapid uplift

773   and exceptional topography of Gongga Shan on the eastern margin of the Tibetan Plateau.

774   *Earth and Planetary Science Letters, 481,* 328–337, doi: 10.1016/j.epsl.2017.10.043

775   Dai, F.C, Lee, C.F., Deng, J.H., & Tham, L.G. (2005). The 1786 earthquake-triggered landslide dam

776   and subsequent dam-break flood on the Dadu River, southwestern China. *Geomorphology, 65,*

777   205–221. Doi:10.1016/j.geomorph.2005.06.011

778   Deng, Q., Zhang, P., Ran, Y., Yang, X., Min, W., & Chu, Q. (2003). Basic characteristics of active

779   tectonics of China. *Science in China, 46*, 356–372. Doi:10.1360/03yd9032

780   Friedrich, A.M., Wernicke, B.P., Niemi, N.A., Bennett, R.A., & Davis, J.L. (2003). Comparison of

781   geodetic and geologic data from the Wasatch region, Utah, and implications for the spectral

782   character of Earth deformation at periods of 10 to 10 million years. *Journal of Geophysical*

783   *Research, 108(B4)*, 2199. Doi:10.1029/2001JB000682

784   Gan, W., Zhang, P., Shen, Z., Niu, Z., Wang, M., Wan, Y., Zhou, D., & Cheng, J. (2007). Present-

785   day crustal motion within the Tibetan Plateau inferred from GPS measurements. *Journal of*

786   *Geophysical Research, 112*, B08416. Doi:10.1029/2005JB004120

787   Gosse, J., & Phillips, F. (2001). Terrestrial in situ cosmogenic nuclides: Theory and application.

788   *Quaternary Science Reviews, 20,* 475–1560. Doi:10.1016/S0277-3791(00)00171-2

789   Guo, R., Zheng, Y., Tian, W., Xu, J., & Zhang, W. (2018). Locking Status and Earthquake Potential

790   Hazard along the Middle-South Xianshuihe Fault. *Remote sensing, 10,* 2048.

791   doi:10.3390/rs10122048

792   Hallet, B., & Putkonen, J. (1994). Surface dating of dynamic landforms: young boulders on aging

793   moraines. *Science, 265*, 937-940. Doi: 10.1126/science.265.5174.937

794   Han, S., Li, H., Pan, J., Lu, H., Zheng, Y., Liu, D., & Ge, C., (2019). Co-seismic surface ruptures

795   in Qiangtang Terrane: Insight into Late Cenozoic deformation of central Tibet.

796   *Tectonophysics, 750*, 359–378. Doi :10.11016/j.tecto.2018.11.001

797 Heyman, J., Stroeven, A.P., Harbor, J., & Caffee, M.W. (2011). Too young or too old: Evaluating

798   cosmogenic exposure dating based on an analysis of compiled boulder exposure ages. *Earth*

799   *and Planetary Science Letters, 302,* 71–80. Doi:10.1016/j.epsl.2010.11.040

800 Heyman, J. (2014). Paleoglaciation of the Tibetan Plateau and surrounding mountains based on

801   exposure ages and ELA depression estimates. *Quaternary Science Reviews, 91*, 30–41.

802   Doi:10.1016/j.quascirev.2014.03.018

803 Ji, L., Zhang, W., Liu, C., Zhu, L., Xu, J., & Xu, X. (2020). Characterizing interseismic deformation

804   of the Xianshuihe fault, eastern Tibetan Plateau, using Sentinel-1 SAR images. *Advances in*

805   *Space Research, 66,* 378–394. Doi:10.1016/j.asr.2020.03.043

806 Jiang, G., Wen, Y., Liu, Y., Xu, X., Fang, L., Chen, G., Meng, G., & Xu, C. (2015a). Joint analysis

807   of the 2014 Kangding, southwest China, earthquake sequence with seismicity relocation and

808   InSAR inversion. *Geophysical Research Letters, 42,* 3273-3281. Doi:10.1002/2015GL063750

809 Jiang, G., Xu, X., Chen, G., Liu, Y., Fukahata, Y., Wang, H., Yu, G., Tan, X., & Xu, C. (2015b).

810   Geodetic imaging of potential seismogenic asperities on the Xianshuihe-Anninghe-Zemuhe

811   fault system, southwest China, with a new 3-D viscoelastic interseismic coupling model.

812   *Journal of Geophysical Research - Solid Earth, 120,* 1855–1873. Doi:10.1002/2014JB011492

813 Kohl, C.P., & Nishiizumi, K. (1992). Chemical isolation of quartz for measurement of in-situ -

814   produced cosmogenic nuclides. *Geochimica et Cosmochimica Acta, 56*, 3583-3587.

815   Doi:10.1016/0016-7037(92)90401-4

816 Lal, D. (1991). Cosmic-ray labeling of erosion surfaces-In situ nuclide production rates and erosion

817   models. *Earth and Planetary Science Letters, 104 (2-4)*, 424–439. Doi:10.1016/0012-

818   821X(91)90220-C

819   Li, Y., & Bürgmann, R. (2021). Partial coupling and earthquake potential along the Xianshuihe

820   Fault, China. *Journal of Geophysical Research*, doi:10.1029/2020JB021406

821   Li, T., Du, Q., Zhang, C., & You, Z., 1997. The Active Xianshuihe Fault Zone and its Seismic

822   Risk Assessment. Chengdu Cartographic Publishing House, Chengdu, 230 pp. (in

823   Chinese)

824   Li, H., & Zhang, Y. (2013). Zircon U–Pb geochronology of the Konggar granitoid and migmatite:

825   constraints on the Oligo-Miocene tectono-thermal evolution of the Xianshuihe fault zone, East

826   Tibet. *Tectonophysics, 606,* 127–139. Doi:10.1016/j.tecto.2013.07.007

827   Li, Z., Xiao, H., & Zhou, B. (2015). Effect of fault steps on propagation and termination behavior of

828   strike-slip earthquake surface rupture. *Seismology and Geology, 37(1),* 126-138 (in Chinese)

829   Li, T., Zhu, Y., Yang, Y., Xu, Y., An, Y., Zhang, Y., Feng, S., Huai, Y., & Yang, J. (2019). The current

830   slip rate of the Xianshuihe fualt zone calculated using mutiple observation data of crustal

831   deformation. *Chinese Journal of Geophysics, 62(4),* 1323-1335 (in Chinese)

832   Li J., Zhou, B., Li, T., Yang, Y., & Li, Z. (2020). Locking depth, slip rate, and seismicity distribution

833   along the Daofu–Kangding segment of the Xianshuihe fault system, eastern Tibetan Plateau.

834   *Journal of Asian Earth Sciences, 193,* 104328. Doi:10.1016/j.jseaes.2020.104328

835   Liang, M., Chen, L., Ran, Y., Li, Y., Wang, D., Gao, S., Han, M., & Zeng, D. (2020). Late

836   Quaternary activity of the Yalahe fault of the Xianshuihe fault zone, eastern margin of the

837   Tibet Plateau. *Seismology and Geology, 42(2),* 513-525. doi:10.3969/j.issn.0253-

838   4967.2020.02.016 (in Chinese)

839   Lifton, N., Sato, T., & Dunai, T.J. (2014). Scaling in situ cosmogenic nuclide production rates using

840   analytical approximations to atmospheric cosmic-ray fluxes. *Earth and Planetary Science*

841   *Letters, 386,* 149-160. Doi:10.1016/j.epsl.2013.10.052.

842   Lin, B., Chen, T., Pu, X., Liu, W., & Peng, M. (1986). Rupture processes of strong earthquakes on

843   Xianshuihe fault belt and seismic activity. *Acta Seismologica Sinica*, 8(1), 1–20. (in Chinese)

844   Lisiecki, L.E., & Raymo, M.E. (2005). A Pliocene–Pleistocene stack of 57 globally distributed

845   benthic δ18O records. *Paleoceanography, 20*, PA1003. Doi:10.1029/2004PA001071

846   Liu, Z., Zhang, G., Hu, Y., & Yang, Y. (1977). Geological map of Gongga (H-47-24). Sichuan

847   Institute of Geology, Scale 1/200,000

848   Lu, Y., Shi, R., Hu, Y., & Zhang, S. (1975). Geological map of Yingjing (H-48-19). Sichuan

849   Institute of Geology, Scale 1/200,000

850   Meade, B. J., & Loveless, J. P. (2009). Block modeling with connected fault network geometries

851   and a linear elastic coupling estimator in spherical coordinates. *Bulletin of the Seismological*

852   *Society of America, 99 (6)*, 3124–3139. Doi:10.1785/0120090088

853   Nalbant, S.S., & McCloskey, J. (2011). Stress evolution before and after the 2008 Wenchuan, China

854   earthquake. *Earth and Planetary Science Letters, 307,* 222–232.

855   Doi:10.1016/j.epsl.2011.04.039

856   Ouimet, W.B., Whipple, K.X., & Granger, D.E. (2009). Beyond threshold hillslopes: chan-nel

857   adjustment to base-level fall in tectonically active mountain ranges. *Geology 37*, 579–582.

858   Doi:10.1130/g30013a.1

859   Pan, J., Li, H., Chevalier, M.L., Bai, M., Liu, F., Liu, D., Zheng, Y., Lu, H., & Zhao, Z. (2020). A

860   newly discovered active fault on the Selaha-Kangding segment along the SE Xianshuihe fault:

861   the South Mugecuo fault. *Acta Geologica Sinica, 94(11)*, 3178-3188 (in Chinese). doi:

862   10.19762/j.cnki.dizhixuebao.2020196

863   Papadimitriou, E., Wen, X., Karakostas, V., & Jin, X. (2004). Earthquake Triggering along the

864   Xianshuihe Fault Zone of Western Sichuan, China. *Pure applied Geophysics, 161,* 1683–1707.

865   Doi:10.1007/s00024-003-2471-4

866 Parsons, T., Ji, C., & Kirby, E. (2008). Stress changes from the 2008 Wenchuan earthquake and

867   increased hazard in the Sichuan basin. *Nature, 454,* 509–510. Doi:10.1038/nature07177

868 Putkonen, J., & Swanson, T. (2003). Accuracy of cosmogenic ages for moraines. *Quaternary*

869   *Research, 59*, 255–261. Doi:10.1016/S0033-5894(03)00006-1.

870 Qiao, X., & Zhou, Y. (2021). Geodetic imaging of shallow creep along the Xianshuihe fault and its

871   frictional properties. *Earth and Planetary Science Letters, 567,* 117001.

872   Doi:10.1016/j.epsl.2021.117001

873 Roger, F., Calassou, S., Lancelot, J., Malavieille, J., Mattauer, M., Xu, Z., Hao. Z., & Hou, L.

874   (1995). Miocene emplacement and deformation of the Konga Shan granite (Xianshui He fault

875   zone, west Sichuan, China): Geodynamic implications. *Earth and Planetary Science Letters,*

876   *130,* 201–216. Doi:10.1016/0012-821X(94)00252-T

877 Searle, M.P., Roberts, N.M.W., Chung, S.-L., Lee, Y., Cook, K.L., Elliott, J.R., Weller, O.M., St-

878   Onge, M.R., Xu, X.-W., Tan, X.-B., & Li, K. (2016). Age and anatomy of the Gongga Shan

879   batholith, eastern Tibetan Plateau, and its relationship to the active Xianshuihe fault.

880   *Geosphere, 12 (3)*, 948–970. Doi:10.1130/ges01244.1

881 Segall, P., & Pollard, D. (1980). Mechanics of Discontinuous Faults. *Journal of*

882   *Geophysical Research, 85(B8),* 4337-4350

883 Shao, Z., Xu, J., Ma, H., & Zhang, L. (2016). Coulomb stress evolution over the past 200 years and

884   seismic hazard along the Xianshuihe fault zone of Sichuan, China. *Tectonophysics, 670,* 48-65.

885   Doi:10.1016/j.tecto.2015.12.018

886 Shan, B., Xiong, X., Zheng, Y., & Diao, F. (2009). Stress changes on major faults caused by Mw7.9

887   Wenchuan earthquake May 12, 2008. *Science in China*, 52, 593–601

888   Shan, B., Xiong, X., Zheng, Y., Jin, B., Liu, C., Xie, Z., & Hsu, H. (2013). Stress changes on major

889   faults caused by 2013 Lushan earthquake and its relationship with 2008 Wenchuan earthquake.

890   *Science in China - Earth Science, 56,* 1169-1176. Doi:10.1007/s11430-013-4642-1

891   Shen, Z., Lu, J., Wang, M., & Bürgmann, R. (2005). Contemporary crustal deformation around the

892   southeast borderland of the Tibetan Plateau. *Journal of Geophysical Research, 110,* B11409.

893   Doi:10.1029/2004JB003421

894   Stone, J. O. (2000). Air pressure and cosmogenic isotope production. *Journal of Geophysical*

895   *Research, 105(B10)*, 23,753–23,759. Doi:10.1029/2000JB900181

896   Tapponnier, P., & Molnar, P. (1977). Active faulting and Cenozoic tectonics of China. *Journal of*

897   *Geophysical Research, 82,* 2905-2930. Doi:10.1029/JB082i020p02905

898   Toda, S., Lin, J., Meghraoui, M., & Stein, R.S. (2008). 12 May 2008 M = 7.9 Wenchuan, China,

899   earthquake calculated to increase failure stress and seismicity rate on three major fault systems.

900   *Geophysical Research Letters*, 35, L17305. Doi:10.1029/2008GL034903

901   Wallis, S., Tsujimori, T., Aoya, M., Kawakami, T., Terada, K., Suzuki, K., & Hyodo, H. (2003).

902   Cenozoic and Mesozoic metamorphism in the Longmenshan orogen: implications for

903   geodynamic models of eastern Tibet. *Geology, 31,* 745–748. Doi:10.1130/g19562.1

904   Wang, E., Burchfiel, B. C., Royden, L. H. Chen, L., Chen, J., Li, W., & Chen, Z. (1998). The

905   Cenozoic Xianshuihe– Xiaojiang, Red River, and Dali fault systems of southwestern Sichuan

906   and central Yunnan, China. *Geological Society of America Special Paper, 327,* 108p.

907   Doi:10.1130/SPE327

908   Wang, E., & Burchfiel, B.C. (2000). Late Cenozoic to Holocene deformation in southwestern

909   Sichuan and adjacent Yunnan, China, and its role in formation of the southeastern part of the

910   Tibetan Plateau. *Geological Society of America Bulletin, 112*, 413–423. Doi:10.1130/0016-

911   7606(2000)112<413:LCTHDI>2.0.CO;2

912   Wang, H., Wright, T.J., & Biggs, J. (2009). Interseismic slip rate of the northwestern Xianshuihe

913   fault from InSAR data. *Geophysical Research Letters, 36,* L03302.

914   Doi:10.1029/2008GL036560

915   Wang, S., Jiang, G., Xu, T., Tian, Y., Zheng, D., & Fang, X. (2012). The Jinhe–Qinghe fault—

916   Aninactive branch of the Xianshuihe–Xiaojiang fault zone, Eastern Tibet. *Tectonophysics, 544-*

917   *545,* 93-102. Doi:10.1016/j.tecto.2012.04.004

918   Wang, W., Qiao, X., Yang, S., & Wang, D. (2017). Present-day velocity field and block kinematics

919   of Tibetan Plateau from GPS measurements. *Geophysical Journal International, 208*, 1088-

920   1102. Doi:10.1093/gji/ggw445

921   Wang, Y., Wang, M., & Shen, Z. (2017). Block-like versus distributed crustal deformation around

922   the northeastern Tibetan plateau. *Journal of Asian Earth Sciences, 140*, 31-47.

923   Doi:10.1016/j.jseaes.2017.02.040

924   Wang, W., Qiao, X., & Ding, K. (2020). Present-day kinematics in southeastern Tibet inferred from

925   GPS measurements. *Journal of Geophysical Research,* e2020JB021305.

926   Doi:10.1029/2020JB021305

927   Wang, M., & Shen, Z. (2020). Present-day crustal deformation of continental China derived from

928   GPS and its tectonic implications. *Journal of Geophysical Research, 125,* e2019JB018774.

929   Doi:10.1029/2019JB018774

930   Wells, D.L., & Coppersmith, K.J. (1994). New empirical relationships among magnitude, rupture

931   length, rupture width, rupture area, and surface displacement. *Bulletin of the Seismological*

932   *Society of America, 84*, 974–1002

933   Wen, X. (2000). Character of rupture segment of Xianshuihe- Zemuhe–Anninghe fault zone,

934   western Sichuan. *Seismology and Geology, 22*, 239–249

935   Wen, X., Ma, S., Xu, X., & He, Y. (2008). Historical pattern and behavior of earthquake ruptures

936   along the eastern boundary of the Sichuan–Yunnan faulted-block, southwestern China. *Physics*

937   *of the Earth and Planetary Interiors, 168 (1–2)*, 16–36. Doi:10.1016/j.pepi.2008.04.013

938   Wilson, C.J.L., & Fowler, A.P. (2011). Denudational response to surface uplift in east Tibet:

939   evidence from apatite fission-track thermochronology. *Geological Society of America Bulletin,*

940   *123*, 1966–1987. Doi:10.1130/b30331.1

941   Xie, Z., Zheng, Y., Liu, C., Shan, B., Riaz, M. S., & Xiong, X. (2017). An integrated analysis of

942   source parameters, seismogenic structure, and seismic hazards related to the 2014 M S 6.3

943   Kangding earthquake, China. *Tectonophysics, 712,* 1-9. Doi:10.1016/j.tecto.2017.04.030

944   Xu, G., & Kamp, P.J.J. (2000). Tectonics and denudation adjacent to the Xianshuihe Fault, eastern

945   Tibetan Plateau: constraints from fission track thermochronology. *Journal of Geophysical*

946   *Research, 105,* 19231–19251.Doi:10.1029/2000jb900159

947   Xu, J., Shao, Z., Ma, H., & Zhang, L. (2013). Evolution of Coulomb stress and stress interaction

948   among strong earthquakes along the Xianshuihe fault zone. *Chinese Journal of Geophysics,*

949   *56(4)*, 1146-1158 (in Chinese). Doi:10.6O38/cjg2O13O41O

950   Xu, J., Shao, Z., Liu, J., & Ji, L. (2019). Coulomb stress evolution and future earthquake

951   probability along the eastern boundary of the Sichuan-Yunnan block. *Chinese Journal of*

952   *Geophysics*, *62(11)*, 4189-4213 (in Chinese)

953   Yan, B., & Lin, A. (2015). Systematic deflection and offset of the Yangtze River drainage system

954   along the strike-slip Ganzi-Yushu-Xianshuihe Fault Zone, Tibetan Plateau. *Journal of*

955   *Geodynamics, 87,* 13-25. Doi:10.1016/j.jog.2015.03.002

956   Yan, B., & Lin, A. (2017). Holocene Activity and Paleoseismicity of the Selaha Fault, Southeastern

957   Segment of the Strike-Slip Xianshuihe Fault Zone, Tibetan Plateau. *Tectonophysics, 694(2),*

958   302–318. Doi:10.1016/j.tecto.2016.11.014

959   Yan, B., Jia, D., & Lin, A. (2018). Late Pleistocene-Holocene tectonic landforms developed along

960   the strikeslip Xianshuihe Fault Zone, Tibetan Plateau, China. *Journal of Geodynamics, 120,*

961   11–22. Doi:10.1016/j.jog.2018.05.005

962   Yan, B., Wang, M., Jia, D., & Cui, J. (2019). Investigation and magnitude re-evaluation of the 1955

963   Zheduotang earthquake, eastern Tibetan Plateau, China. *Geological Journal, 2019,* 1–13.

964   Doi:10.1002/gj.3628

965   Yang, W., Cheng, J., Liu, J., & Zhang, X. (2015). The Kangding earthquake swarm of November,

966   2014. *Earthquake Science, 28(3)*, 197-207. Doi:10.1007/s11589-015-0123-2

967   Zechar, J.D., & Frankel, K.L. (2009). Incorporating and reporting uncertainties in fault slip rates.

968   *Journal of Geophysical Research, 114*, B12407. Doi:10.1029/2009JB006325

969   Zhang, Y., Chen, W., & Yang, N. (2004). 40Ar/39Ardating of shear deformation of the Xianshuihe

970   fault zone in west Sichuan and its tectonic significance. *Science in China, 47*, 794–803.

971   Doi:10.1360/03yd0509

972   Zhang, P.Z. (2013). A review on active tectonics and deep crustal processes of the Western Sichuan

973   region, eastern margin of the Tibetan Plateau. *Tectonophysics, 584,* 7-22.

974   Doi:10.1016/j.tecto.2012.02.021

975   Zhang, Y., Replumaz, A., Leloup, P.H., Wang, G., Bernet, M., van der Beek, P., Paquette, J.L. &

976   Chevalier, M. L. (2017). Cooling history of the Gongga batholith: implications for the

977   Xianshuihe Fault and Miocene kinematics of SE Tibet. *Earth and Planetary Science Letters,*

978   *465,* 1-15. Doi:10.1016/j.epsl.2017.02.025

979   Zhang, L., Cao, D., Zhang, J., & Sui, L. (2019). Interseismic Fault Movement of Xianshuihe Fault

980   Zone Based on Across-Fault Deformation Data and InSAR. *Pure and Applied Geophysics,*

981   *176*, 649–667. Doi:10.1007/s00024-018-1989-4

982   Zheng, G., Wang, H., Wright, Tim J., Lou, Y., Zhang, R., Zhang, W., Shi, C., Huang, J., & Wei, N.

983   (2017). Crustal deformation in the India-Eurasia collision Zong from 25 years of GPS

984   measurements. *Journal of Geophysical Research, 122*, 9290–9312.

985   Doi:10.1002/2017JB014465

986   Zhou, R., He, Y., Huang, Z., Li, X., & Yang, Z. (2001). The slip rate and recurrence of strong

987   earthquakes of Qianning-Kangding segment, the Xianshuihe fault zone. *Acta Seismologica*

988   *Sinica, 23(3),* 250-261 (in Chinese)

989

990   **Figure Captions for Supplementary material:**

991   **Figure S1.** Photos of boulders collected for [10]Be surface-exposure dating at the ZDT

992   moraine site with their approximate sizes.

993

994   **Figure S2:** Photos of boulders collected for [10]Be surface-exposure dating along the MX main

995   moraine with their approximate sizes.